The Dissertation Committee for David Matthew Walker Certifies that this is the approved version of the following dissertation:

The Role of Electrostatic Fields in Ras-Effector Binding and Function

Committee:

Lauren Webb, Supervisor

Adrian Keating-Clay

Kenneth A. Johnson

David Hoffman

Pengyu Ren

The Role of Electrostatic Fields in Ras-Effector Binding and Function

by

David Matthew Walker, B.S. Chem

Dissertation

Presented to the Faculty of the Graduate School of

The University of Texas at Austin

in Partial Fulfillment

of the Requirements

for the Degree of

Doctor of Philosophy

The University of Texas at Austin

May 2014

Dedication

For my mother and father, and the future generations that will use this research.

The Role of Electrostatic Fields in Ras-Effector Binding and Function

David Matthew Walker, Ph D.

The University of Texas at Austin, 2014

Supervisor: Lauren Webb

The organization of two or more biological macromolecules into a functioning assembly is critical for many biological functions to occur. This phenomenon is the result of subtle interplay between complimentary structural and electrostatic factors. While a growing protein data bank of solved protein structures provides experimental evidence for studying the structural factors that stabilize protein-protein interface, there has been little advance in experimental determination of the electrostatic contributions. This lack of experimental investigation into protein electrostatics results in an inability to describe or predict how protein-protein complexes are arranged and stabilized. This problem is addressed in this dissertation by use of vibrational Stark effect (VSE) spectroscopy in which the spectral transitions of a vibrational probe are directly related to the strength and direction of the electric fields in the vicinity of the probe. The work presented here details an approach using VSE spectroscopy coupled with molecular dynamics simulation (MD) to interpret the role that electrostatics play in organizing the signaling protein Ras' interactions with its downstream effectors Raf and Ral guanosine dissociation simulator (RalGDS). Each chapter describes a specific set of experiments and MD simulations designed to understand the nature of protein-protein interactions. In Chapter 3, changes in the absorption energy of the nitrile probe at nine positions along the Ras-Ral interface

were compared to results of a previous study examining this interface with Ral-based probes, and a pattern of low electrostatic field in the core of the interface surrounded by a ring of high electrostatic field around the perimeter of the interface was found. The areas of conserved Stark shifts are used to help describe electrostatic factors that stabilize the Ras-Ral interface. In Chapter 4, VSE is used to describe an electrostatic origin to the binding tilt between complexes formed between Ras and its two effectors Raf and Ral. There are three regions of conserved Stark effect shifts upon docking with WT Ras between the two effectors, indicating that the docked complexes conserve electrostatic fields, resulting in different binding orientation of otherwise structurally similar proteins. Chapter 5 details the use of MD simulation in correlation with VSE data for 18 mutants of the Ras at the oncogenic position 61 site. The combination of experimental and simulations support the hypothesis that position 61 on Ras is used to coordinate an active site water molecule during native guanosine triphosphate (GTP) hydrolysis.

Table of Contents

List of Tables

List of Figures

Chapter 1 Introduction

Many biological processes are dependent on the formation of stable protein-protein complexes. Shown in Figure 1-1 is a detailed example of a few of the cellular signaling pathways involved in eukaryotes. It is important to note that each arrow represents specific noncovalent protein-protein interactions. For cellular viability, these interactions must be organized with a high degree of fidelity in a timely and effective manner. The tools that nature has evolved to use in organizing these interactions are a complex convolution of structure and electrostatics. Techniques such as x-ray crystallography and NMR are being used to elucidate how certain structural factors such as hydrogen bonds, salt bridges, and hydrophobic interactions that help stabilize protein-protein interaction. While these techniques give much needed structural insight into the formation of protein-protein complexes, they fail to provide predictive capabilities to describe unobserved protein-protein interactions in detail *a priori*. While a growing protein data bank of solved protein structures provides experimental evidence for studying the structural factors that stabilize protein-protein interface, there has been little advance in experimental determination of the electrostatic contributions.

Vibrational Stark effect (VSE) spectroscopy is a powerful tool for studying electrostatic fields in proteins.[1-3] The vibrational Stark effect is a measurement of the change in a vibrational chromophore's spectral profile due to changes in local electrostatic fields. This behavior is describe below in Equation 1-1:

$$hc\Delta\bar{\nu}_{obs} = -\Delta\vec{\mu} \bullet \vec{F} \qquad (1\text{-}1)$$

where the change in absorption energy of a vibrational probe ($\Delta\bar{\nu}_{obs}$) is related to changes of the local electrostatic fields ($\vec{F}$) through a negative dot product of the difference dipole of the reporter molecule ($\Delta\vec{\mu}$) (as well as Plank's constant, *h*, and the speed of light, *c*). When using VSE to study protein – protein docking, a probe is typically covalently attached to the surface of one of the proteins. The surface of the protein is a complex arrangement of a heterogeneous electrostatic topology that generates its own electrostatic fields that cannot be "turned off." Therefore any observable electrostatic change is due to a convolution of electrostatic fields from all contributing sources including proteins during docking, and solvent interactions. To account for this more complex environment, Equation 1-1 is more accurately expressed as Equation 1-2.

$$hc\Delta\bar{\nu}_{obs} = -\Delta\vec{\mu} \bullet \Delta\vec{F}_{protein} \qquad (1\text{-}2)$$

The changes in absorption energy ($\Delta\bar{\nu}_{obs}$) are measured as changes from a reference state to a perturbation state as shown below in Figure 1-2. The result of the energy shift is dependent on the strength of the electrostatic field change ($\Delta\vec{F}_{protein}$), and the direction of the difference dipole ($\Delta\vec{\mu}$) with respect to the field. In instances where field change is parallel to the difference dipole, absorption energy is decreased (shown in red). When the difference dipole is anti-parallel to the field change, absorption energy is increased (shown in blue). When studying electrostatic fields of protein-protein interactions, a suitable vibrational oscillator is placed on the surface of a protein at or near the interfacial region of the complex. In the work detailed within, the reference state is a monomeric solution of a nitrile labeled protein without its binding partner. The perturbation state

spectrum is acquired when a solution of the VSE labeled protein and its binding partner are allowed to reach a binding equilibrium. Any differences between the reference and perturbation spectrum need to be carefully reviewed through computational and kinetic experiments to determine if $\Delta\bar{\nu}_{obs}$ arises from changes in local electrostatics due to binding.

When designing Stark effect experiments, it is important to select a convenient probe to measure. For the probe to be a successful reporter of electrostatic fields it must meet certain criteria:[3-4] 1) It must absorb in a clear region of the vibrational spectrum. This is complicated due to the overly complex vibrational profile within proteins that contain many varying chemical groups in their side chains. 2) The probe must exhibit a high molar absorptivity to avoid the need for over concentration and protein aggregation. 3) The probe needs to be sensitive to field changes to measure subtle changes in local fields. This attribute is directly measured by the probes difference dipole moment ($\Delta\vec{\mu}$ presented in equation 1-2). 4) The probe must be stable in an aqueous solution. 5) The probe must make minimal changes to the proteins being studied. 6) The probe must be able to be placed with high specificity within the system of interest. To satisfy each of these criteria, the nitrile was selected as the most efficient Stark probe for investigating protein-protein interactions. The nitrile has been previously investigated as a Stark probe and is known to have a relatively large difference dipole ($\Delta\vec{\mu}$ = 0.7 cm^{-1}/(MV/cm)).[4] A facile method for specific placement of the nitrile has been developed[5] and is shown in Figure 1-3. The labeling of a protein involves the chemical modification of surface

cysteines through a two-step reaction with dithionitrobenzoic acid (DTNB) followed by treatment with potassium cyanide.

As presented in Equation 1-2 and described by Figure 1-2, the extent of change in absorption energy is dependent on the strength of the change in electrostatic fields projected unto the nitrile's bond axis. This leads to the conclusion that electrostatic fields can only be described to the extent to which the nitrile's geometric distribution is known. In the case of studying proteins in solution, each spectrum represents an ensemble of various structural components which need to be accounted for during interpretation. This is typically achieved through molecular dynamics (MD) simulation of the system of interest to generate the Boltzmann-weighted ensemble of structures expected to be present during physical experimentation. Because protein simulation, especially those involving explicit waters, can reach 10's or 100's of thousands of atomistic interactions, the ability to sample structures adequately becomes a difficult task. In this dissertation this was overcome by use of an advanced umbrella sampling technique,[6] by which biasing potentials where applied to the simulation to help the nitrile sample space in a reasonable time frame. To this end, each VSE experiment presented herein is supplemented by the necessary MD simulations for interpretation, and lead to interesting conclusions presented later in this document.

The oncoprotein protein $p21^{Ras}$ (hereafter called "Ras") has been the subject of intense study for the past few decades.[7-8] Ras is a GTPase that is involved in multiple signaling transduction cascades that are vital to cell growth and function. Its connection to cellular growth and replication has made Ras the subject of intense oncological

research.[9-11] It is reported that mutations to Ras are found in 30% of human tumor cells.[12] Ras is the canonical member of the superfamily of Ras-like GTPases which share similar structural characteristics shown in Figure 1-4 as well as many of the same binding partners.[13-14] Structurally, many of the GTPases in this family share a guanosine triphosphate (GTP) binding site. Located near the active site of the protein are the unstructured coils that are designated as the switch I region comprised of residues 28 to 39 (shown below the GTP molecule in Figure 1-4) and the switch II region comprised of residues 59 to 67 (shown to the right of the GTP molecule in Figure 1-4).[13,15-16] These domains are of particular interest because they serve as the primary interacting domains of Ras with its downstream effectors. The GTP hydrolysis cycle shown in Figure 1-5 provides a convenient mechanism for Ras to control levels of cellular signaling. Ras' signal propagation is dependent on the molecule bound to the active site of Ras. In the ON stage there is a bound GTP molecule that lets Ras assume certain conformations to signal with its downstream effectors. Typically the GTP is hydrolyzed with the aid of a GTPase activating protein (GAP), and signaling is turned off. Ras is then primed for the exchange of guanosine diphosphate (GDP) in its active site with GTP to start signaling once again. With this picture of how Ras functions as a biological mediator for signaling, the need to be able to describe the physical origins for the selective interactions of Ras with multiple binding partners becomes apparent. As a signaling protein, its function is dependent on the timely, selective, and effective interaction with other proteins in the signaling pathway known as effectors. A handful of these effectors are shown in Figure 1-6. Although Ras has been shown to be an important component in many signaling

pathways, it demonstrates a selective behavior to interact with the appropriate effector. Several such downstream effectors are c-Raf-1 (hereafter "Raf") to initiate the MAPkinase cascade for cell division,[14] phosphatidylinositol 3-kinase (PI3K) to promote transcription and cytoskeletal signaling,[11,17] and Ral guanine nucleotide dissociation stimulator (RalGDS, hereafter called "Ral") to promote vesicle transport.[10,18-19] While this binding discrimination is partially attributed to different isoforms of Ras and cellular location *in vivo, in vitro* studies have shown that Ras can selectively differentiate between downstream effectors independently of cell location (dissociation constants of ~18 nM,[20-21] ~1 μM,[20,22] and ~3.2nM[23-24] for Raf, Ral, and PI3K, respectively) and therefore must have a noncovalent mechanism to identify and dock with the appropriate downstream effector. Interestingly crystal structures of these downstream effectors have shown similar ubuquitin-like folds, and the largest backbone root means squared deviation (RMSD) between any two effectors is fewer than 4 Å.[16] The structural similarities between the downstream effectors Raf and Ral are shown below in Figure 1-7. Despite the striking similarities in structure, Raf and Ral, the two most heavily studied downstream effectors share no discernible sequence identity as determined by protein BLAST.[25] Additionally crystal structures of a Raf bound to the structural homolog of Ras, Rap1A, show a measureable tilt in binding orientation to that seen in the crystal structures of a Ras – Ral complex. This binding tilt is shown below in Figure 1-8. The origins of the tilt have been described as a need to maintain the same number of overall hydrophobic and hydrophilic interactions between Ras and its effector.[16,26-27] This purely structural assessment is convenient for cases in which the structures of the complexes are

solved, but fails to describe protein-protein interactions where there is no crystallographic data such as the Ras – PI3Kγ complex. Given the structural similarities between the effectors we hypothesize that the binding discrimination exhibited by Ras is electrostatic in origin. This makes the Ras system is an ideal candidate to study the role electrostatics play in organizing and selecting biological interactions between two proteins in a system where structural contributions are controlled to the greatest extent possible.

Overall, the work presented here is the focus of three studies using the Ras – effector system of proteins. In all cases a combination of VSE measurements and MD simulation was used to investigate the behavior of Ras and its effectors. In Chapter 3 investigations of the Ras – Ral interface from the side of Ras demonstrate a conserved ring of high energy Stark effect shifts on both sides of the interface. This conservation of Stark patterns immediately suggests a model in which Ras can recognize, organize, and stabilize interactions between its downstream effectors. In Chapter 4 an in-depth investigation of the Ras – Raf complex interface from the side of Raf provides an expanded data set to compare other VSE experiments done on the Ras – Ral complex. The observation of very distinct patterns of conserved Stark effect shifts between the two complexes support the hypothesis of an electrostatic origin to the differential binding tilt between Ras and its two effectors. Additionally this provides the foundations for a model that allows for the detailed physical description of protein-protein interactions in cases where known structure is absent. Finally, in Chapter 5 VSE was used to show a correlation between the solvent accessible surface area (SASA) of any residue mutation at position 61 on Ras. These observations help support the hypothesis that position 61 is

involved in interactions with active site waters for the hydrolysis of GTP, and helps describe the oncogenic behavior of position 61 mutations to Ras.

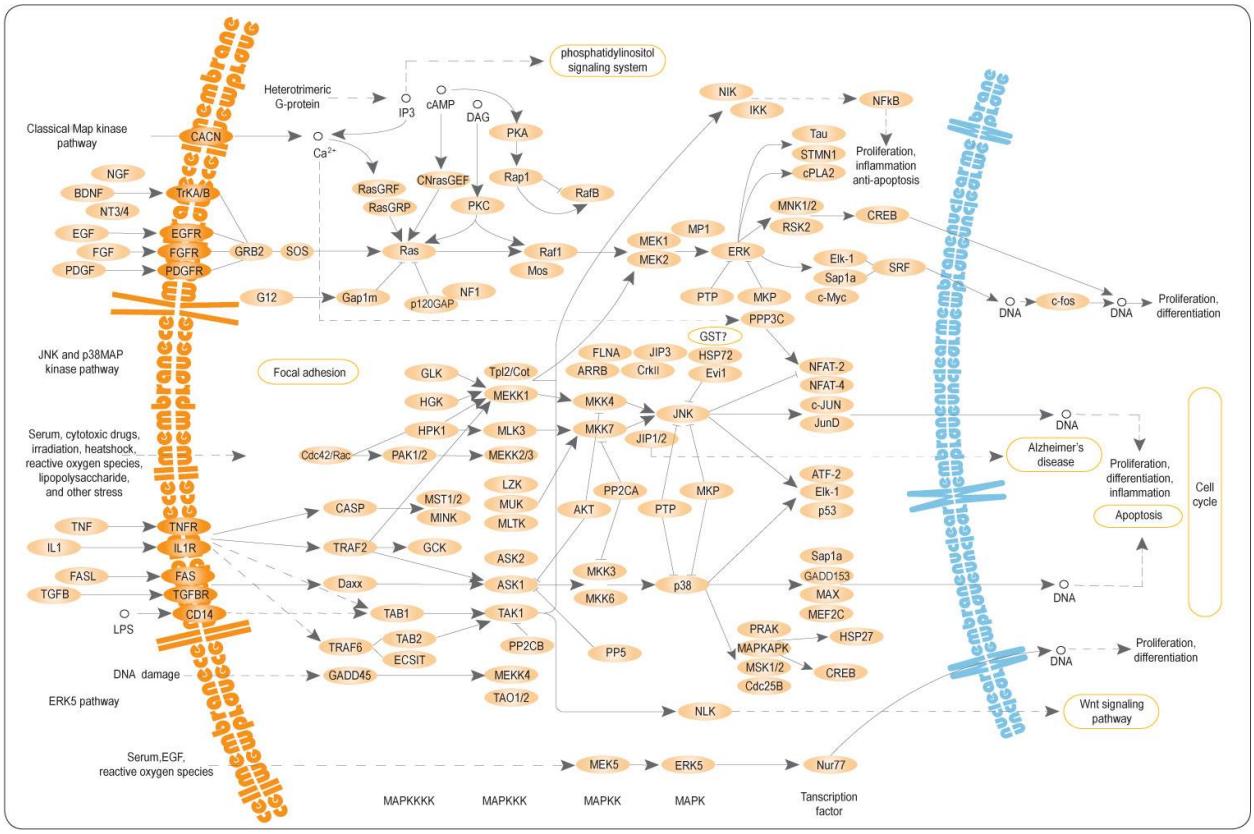

Figure 1-1 MAPk pathways

Demonstration of the complexity of cellular signaling pathways. Each arrow in the figure represents specific protein-protein interactions that most occur in a timely and effective manner for biological processes to occur. Adapted from Wikimedia Commons file "image:MAPKpathway.jpg" under the open content license

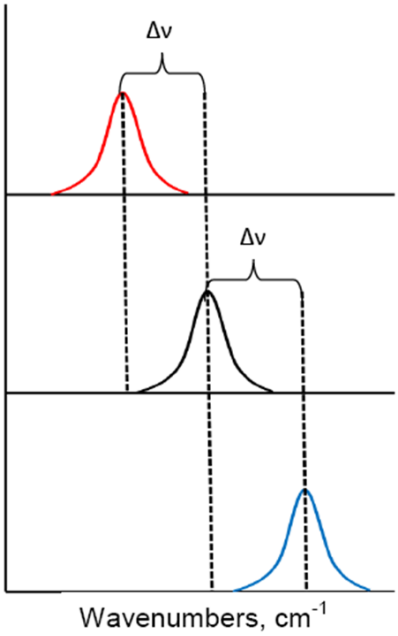

Figure 1-2 Explanation of VSE experiments

Vibrational Stark effect spectroscopy is a measurement of the influence local electrostatic fields have on the vibrational energy of an oscillator. Often a reference spectrum (shown in black) is measured against a perturbation state spectrum.

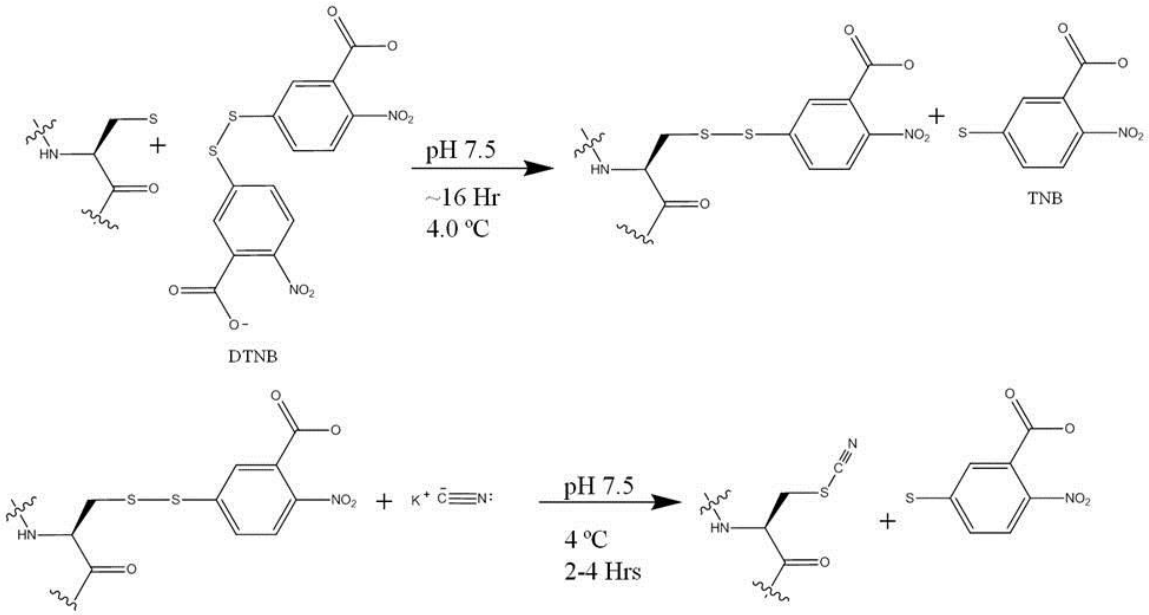

Figure 1-3 Chemical modification of surface cysteines

A nitrile probe can be placed on the surface of a protein in a facile two step process. In the first step, reduced surface cysteines are reacted with DTNB. Reaction with DTNB can be monitored by UV absorbance to completion. In a second step, the disulfide cytokine-TNB intermediate is reacted with potassium cyanide to form the nitrile labeled cyanocysteine. Once again TNB release can be monitored by UV absorbance.

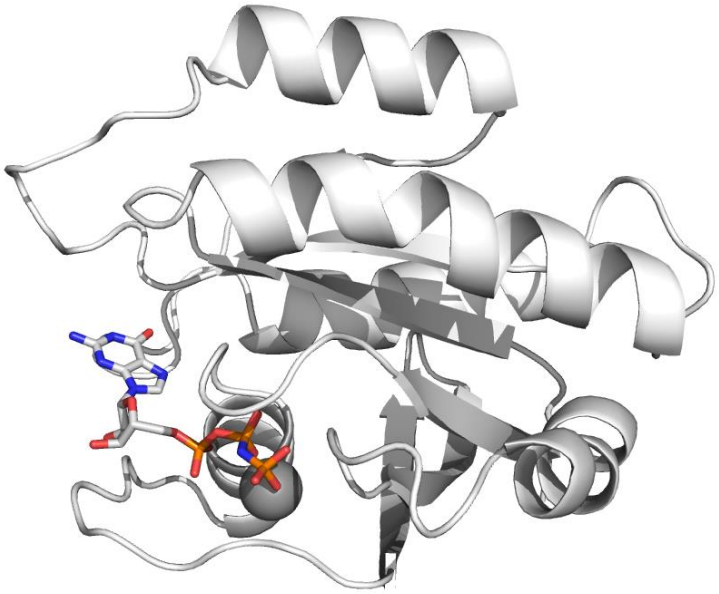

Figure 1-4 Ras structure
Crystal structure of Ras taken from 1LFD.[28] The Ras structure has certain elements belonging to many of the GTPases within the family.

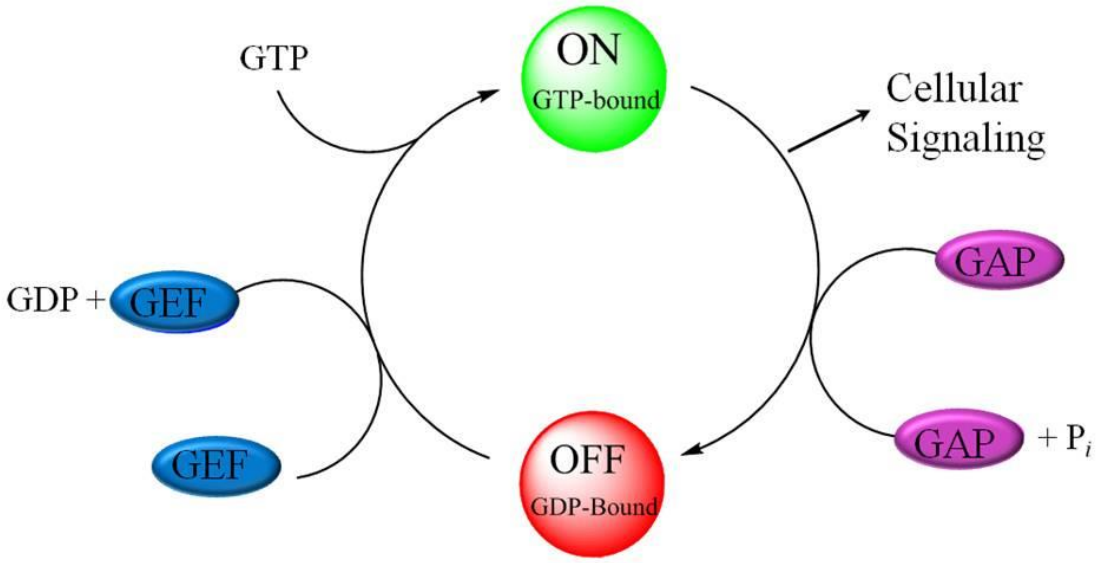

Figure 1-5 Ras GTPase cycle

Ras' ability to communicate in signaling pathways is dependent on the molecule bound in its active site. In the case where GTP is bound Signaling can occur. Upon GTP hydrolysis signaling is turned "off". The GDP must be replaced by GTP to turn signaling back "on".

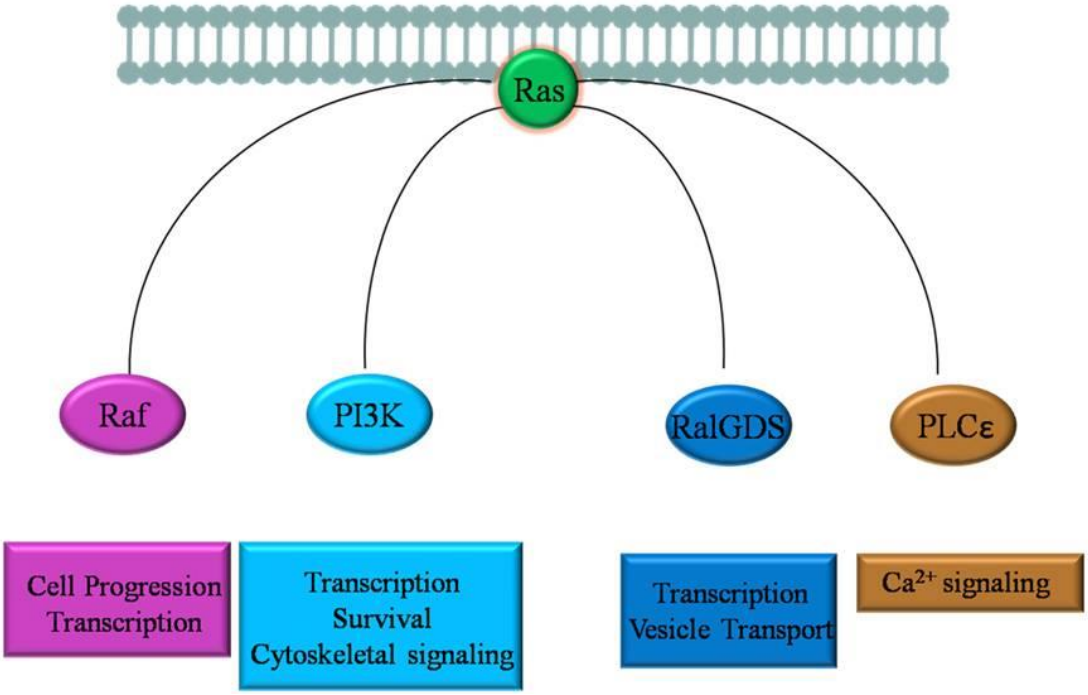

Figure 1-6 Ras' downstream effectors

The GTPase Ras is known to be involved in multiple cellular signaling pathways. The outcome of each of these pathways is dependent on interacting with the correct down-stream effector.

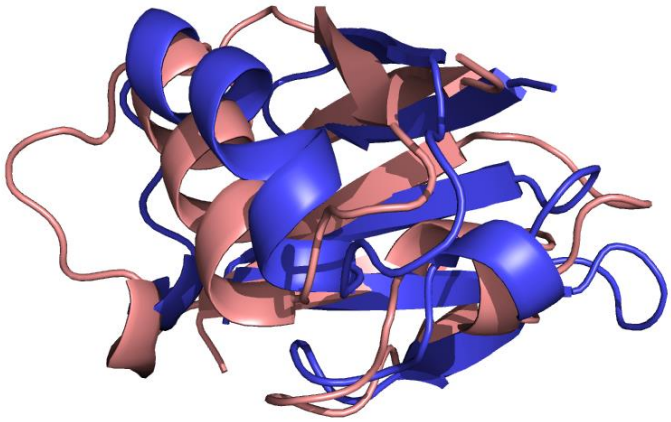

Figure 1-7 Structural overlay of Raf and Ral

Structural alignment of Ras' downstream effectors Raf (blue) and Ral (salmon). The overall ubuquitin-like fold represents a backbone RMSD of 3.6 Å between the two proteins.

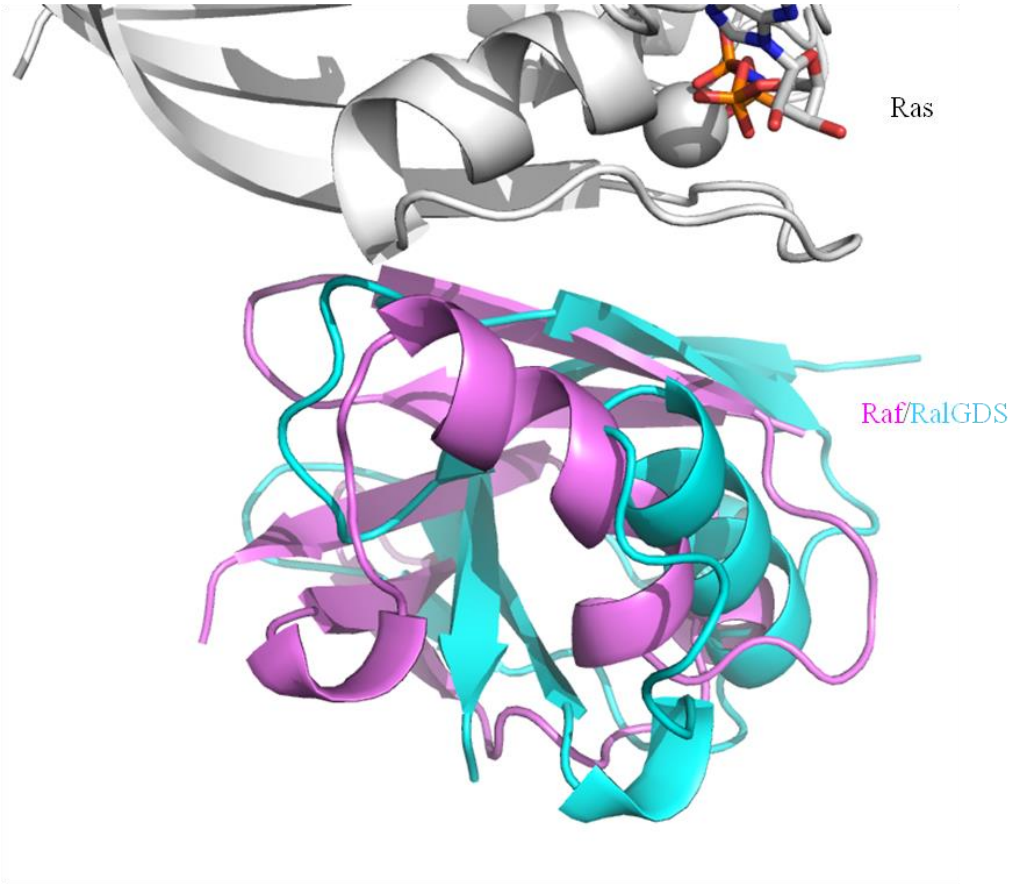

Figure 1-8 Effector binding tilt differentiation

There is a noticeable difference in binding orientation between the of Ras – Ral and the Ras homolog Rap1A – Raf complexes. The orientation of Ral (cyan) with respect to Raf (pink) is calculated as a 35º tilt. This tilt has been described by structural techniques as the need to preserve the same overall number of hydrophobic and hydrophilic interactions between the two surfaces.

Chapter 2 Experimental Methods

2.1 Design, Expression, Growing, and Labeling of Proteins

2.1.1 *Rasβ Construct Design*

The pProEx-Htb expression vector containing wild-type H-Ras residues 1-166 was taken from a previous study in our laboratory. [22]The plasmid was selective for ampicillin resistance and contained a 6x-histadine tag linked to the N-terminal end of the Ras construct with a Tobacco etch virus (TEV) protease site. Amino acid mutations were made via the Stratagene Quick change mutagenesis kit with PCR primers obtained through Sigma-Aldrich. The Ras construct contained three wild-type (WT) cysteine residues, C51, C80, and C118. These cysteines were mutated to alanines, generating a cys-less construct hereafter referred to as Rasβ. Nine residues at the surface of Ras that become immersed in the Ras-effector binding interface were identified from the crystal structure 1LFD:[27] I21, Q25, H27, V29, E31, D33, I36, S39, and Y40. These locations are highlighted below in Figure 2-1. These residues were individually mutated to cysteine to generate nine Rasβ mutants. The wild type and single cysteine Rasβ plasmids were transformed into competent BL21(DE3) *Eschericia coli* cells (Novagen) for expression and purification by heat shock.

Cultures containing the pProEx Hb vector were identified through ampicillin resistance screening, and were placed in a 5 mL terrific broth solution with 100 μg ampicillin/ml (TB/amp) shaking overnight at 37 ºC. The 5 mL solution was then used to inoculate a 250 mL TB/amp solution. The inoculated solution was allowed to grow at 37 ºC while shaking until an OD at 600 nm (OD_{600}) of 0.6 was observed (typically 2-3

hours). The 250 mL of healthy cells where then distributed amongst 6 2L TB/amp flasks for growing at 37 ºC while shaking. Cell growth was monitored until an OD_{600} of 0.6 was achieved (typically 4-5 hours). Protein expression was induced by adding isopropyl β-D-1-thiogalactopyranoside (IPTG, Sigma-Aldrich) to 1 mM concentration. The temperature was reduced to 18 ºC and expression was carried out over 16 h while shaking.

Cells were collected by centrifugation at ~9000 RCG for 30 minutes at 4 ºC and the supernatant was discarded. The pellets were resuspended in a lysis buffer containing 50 mM phosphate pH 8.0, 500 mM NaCl, and 20 mM immidizole. The resuspended cells were lysed by sonication as described in literature.[22,29-30] The lysate was centrifuged at ~31000 RCG for 45 minutes at 4 ºC and the supernatant was collected for purification. The lysate was passed through a 2 μm filter then added to a Ni-nitrilotriacetic acid (Ni-NTA) column for affinity chromatography. After washing, the histidine tagged protein was eluted from the column using an immidzole gradient from 20 mM to 500 mM immidazole, and exchanged into a TEV protease buffer of 50 mM Tris pH 8.0, 50 mM KCl, and 10% glycerol. Ras concentration was estimated by absorbance at 280 nm. TEV protease with an N-terminal histadine tag was added to the protein solution at 1 mg TEV per 10 mg Ras. The TEV protease reaction occurred over 12-14 hours at 4 ºC to remove the histidine tag from the N-terminus of Ras. After his-tag cleavage reaction, immidizole was added to the solution to a final 20 mM concentration and the solution was run through a Ni-NTA column collecting the eluent. Following elution from the Ni-NTA column, Ras was solvent exchanged into an experimental buffer of 50 mM Tris, 100 mM

NaCl, and 10% glycerol using a desalting column, and protein concentration was estimated using UV absorbance at 280 nm.

After purification, the WT Ras and Rasβ mutants were loaded with the nonhydrolyzable GTP analog guanosine 5'-[*β*,*γ*-imido]triphosphatetrisodium salt hydrate (GDPNP, Sigma) to maintain the protein in the GTP-bound ON state for effector binding. This was done by adding EDTA to the protein solution to a final 2 mM concentration and adding 1.2 molar equivalents of GDPNP. GDPNP exchange was carried out at room temperature for 2 hours, and then $MgCl_2$ was added to a final 5 mM concentration. The GDPNP loaded Ras protein was then solvent exchanged into 50 mM Tris, 100 mM NaCl, and 10% glycerol using a pd-10 desalting column. Yields for the Rasβ mutants were typically 15-20 mg protein per liter of growth media. All spectroscopic data for Rasβ mutants were obtained in a buffer of 50 mM Tris pH 7.5, 100 mM NaCl, and 10% glycerol.

Each of the nine Rasβ mutants were chemically modified with a thiocyanate Stark probe for VSE measurements. The two step process of chemical modification is presented in Figure 1-3. Three molar equivalents of *bis*-thionitrobenzoic acid (DTNB, Aldrich) was added to the protein and allowed to react for 12-16 hours at 4 ºC. The reaction was monitored by increase in the absorbance of the side product, thionitrobenzoic acid, at 412 nm. After one molar equivalent of DTNB had reacted, three molar equivalents of potassium cyanide (KCN, Aldrich) were added to the solution. The reaction was carried out at room temperature, and again the thionitrobenzoic acid absorbance was monitored by UV absorbance at 412 nm until completion, typically 2-4

hrs. The protein was then exchanged into fresh buffer consisting of 50 mM Tris pH 7.5, 100 mM NaCl, and 10% glycerol using a pd-10 desalting column (GE Healthcare). Herein we identify each thiocyanate-labeled Rasβ mutant with the subscript "SCN." The protein was then concentrated to 2 mM by centrifugation for infrared spectroscopy studies.

2.1.2 *Rafβ Constructs Design*

The gene for the Ras binding domain (RBD) of c-Raf-1 with a N-terminal hexahistadine tag linked to the protein by a thrombin cleavage site was purchased on a pET-15b vector from Genscript. The three wild type cysteines (C81, C95, C96) were mutated to alanine through PCR mutagenesis (Qiagen) to construct a "cysless" variant of the protein, hereafter referred to as Rafβ. Eight sites along the RBD (R59C, N64C, K65C, Q66C, T68C, V69C, K84C, and G90C) and one 20 Å away (S77C) were individually mutated to cysteines through PCR mutagenesis. These probe locations are indicated below in Figure 2-2. Except for S77C, these sites were chosen because of their proximity to the protein-protein interface upon binding with Ras. For clarity, we are using the numbering scheme for residue positions found in the PDB entry 1GUA.[26] The purified single cysteine-containing Rafβ plasmids were transformed into competent BL21(DE3) *E. coli* cells (EMD) for expression and purification as described previously. Bacterial cells containing either WT or mutant pET-15b Rafβ plasmids were selected through ampicillin resistance screening for further expression.

The cells containing the pET-15b plasmid were inoculated into 5 mL terrific broth (TB) media and grown at 37ºC while shaking for 14-16 hours. The 5 mL growth was then

used to inoculate 250 mL of TB. The 250 mL culture was grown at 37 ºC while shaking until an OD_{600} of 0.6 was achieved, and then used to inoculate 6 2 L flasks of sterilized TB. The 2 L growths were incubated at 37 ºC under shaking until an OD_{600} of 0.6 was achieved. Isopropyl β-D-1-thiogalactopyranoside (IPTG, Sigma-Aldrich) was added to the growths to a concentration of 1 mM and protein expression was carried out at 30ºC while shaking for 6 hours.

Cell collection and lysing for WT Raf and Rafβ constructs was carried out as previously described in this document for the Ras constructs. The hexahistidine tagged Raf constructs were purified from lysate using a Ni-NTA column exactly as described for Ras. After purification from lystate, the protein was transferred into a thrombin cleavage buffer containing 20 mM Tris pH 8.0, 150 mM NaCl, and 2.5 mM $CaCl_2$.

The concentration of the Rafβ product was estimated by absorbance at 280 nm, and thrombin (EMD) was added to the protein solution at a concentration of 2 U per mg of Rafβ. The thrombin cleavage reaction was carried out overnight at 4ºC. The cleavage reaction was run through a benzamidine column pre-equilibrated in the cleavage buffer, and the Rafβ construct was collected in the flow through. The single cysteine-containing Rafβ construct was then exchanged into the final experimental buffer of 50 mM Tris pH 7.5 and 100 mM NaCl. Typical yields from purification were 20-30 mg protein per liter of growth media.

Single cysteine Rafβ constructs were chemically labeled with a nitrile after purification in a two-step process. First 100 mM DTNB in the experimental buffer was added to the protein solution in 1.5 molar equivalents at 4 ºC for 12-16 hours.

Thionitrobenzoic acid release was monitored at 412 nm to ensure a 1:1 stoichometric reaction occurred. After the DTNB reaction, 10 M potassium cyanide was added to the reaction in a 3 molar equivalents to the protein at room temperature for 1 hour. The reaction was followed by observing absorbance at 412 nm to ensure complete labeling of the protein. The labeled protein was solvent exchanged into 50 mM Tris pH 7.5 and 100 mM NaCl buffer using a pd-10 desalting column to remove excess KCN, and side products of the labeling reactions. Nitrile labeling was confirmed using ESI-MS.

2.1.3 *Wild Type Ral*

Wild type Ral purification was carried out as described by Stafford *et al* [22].

2.2 Vibrational Stark Effect Spectroscopy

Infrared spectra were collected with a Bruker Vertex 70 Fourier transform infrared spectrometer using a sample chamber composed of two sapphire windows separated by 125 μm polytetrafluoroethylene (PTFE) spacers. Spectra composed of 250 scans were collected at 0.5 cm^{-1} resolution using a scan range of 2000 cm^{-1} to 2500 cm^{-1} selected by a broad band pass filter and detected by a liquid N_2-cooled indium antinomide (InSb) detector. Relatively high concentrations of the nitrile-labeled protein, ~2 mM, were needed to achieve a suitable signal-to-noise ratio. The background-subtracted peaks were analyzed using an in-house routine which fit the baseline to a third order polynomial using a non-linear least squares method, then used alternating steepest decent and conjugate gradient algorithms to fit the thiocyanate peak to a Gaussian distribution. Experimental error is reported as the standard deviation from at least three replicates.

2.2.1 *Rasβ*

Vibrational Stark effect experiments for the monomer and docked Rasβ proteins were carried out in 50 mM Tris pH 7.5, 100 mM NaCl, and 10% glycerol buffer. Glycerol was added to the buffer to help with stability of the labeled Ras mutants in high concentrations. Docked experiments were performed by adding 1.3 molar equivalents of WT Ral to labeled Ras and let sit at 4 ºC for 1-2 hours to ensure saturated binding of the Rasβ constructs.

2.2.2 *Rafβ*

Monomer and docked Rafβ VSE experiments were done in a 50 mM Tris, 100 mM NaCl buffer. Docked experiments were performed by adding 1.3 molar equivalents of WT Ras to the labeled Raf protein and letting the binding equilibrate at 4 ºC for 1-2 hours.

2.3 Guanosine Dissociation Inhibition Assay

The addition of any functional group to a protein side chain presents a chance for disrupting protein structure or function. Even though the diatomic nitrile is one of the smallest chromaphores that can be added to a protein, it is important to check that the mutations to the β constructs and subsequent chemical modifications do not perturb the system. To establish that the labeled mutants are adequate representations of wild type (WT) interactions the guanosine dissociation inhibition (GDI) assay was used to assess the conservation of interactions between Ras and either of its effectors. Experimental dissociation (K_d) constants between Ras and the two downstream effectors Ral and Raf were obtained through the GDI assay. WT –WT interactions between the GTPase –

effector were compared to the WT – mutant or mutant – WT complexes to determine the effect of labeling the protein to its function.

A 100 nM Ras solution (depending on the experiment this was either WT or a labeled mutant) was loaded with the fluorescently labeled GTP analog 2'-(or 3')-*O*-(*N*-methylanthraniloyl)guanosine 5'-triphosphate trisodium salt (mant-GTP, Invitrogen). The Ras was incubated with concentrations of effector (depending on the experiment this was either a WT or labeled mutant construct) ranging from 0 to 150 nM at 4 ºC for 2-16 hours in a 96 well top reading fluorescence plate (Microfluor). Mant-GTP release was stimulated by the addition of 250 mM GDPNP by gentle pipetting for 10 seconds before recording fluorescence decay of mant-GTP release. Fluorescence was recorded in a multimode top-down fluorimeter (Beckman Coulter Spectra Max M3) using top-down intensity. Excitation and emission wavelengths of the mant-GTP were monitored at 365 and 450 nm respectively. Initial velocities of fluorescence decay were fit to linear curves to obtain k_{obs} which was then used in equation 2-1 to determine K_d.

$$k_{obs} = k_{-1} - k_{-1} * \frac{R_0 + E_0 + K_d - \sqrt{(R_0 + E_0 + K_d)^2 - 4R_0E_0}}{2R_0} \qquad (2\text{-}1)$$

In equation 2-1 k_{-1} is the k_{obs} recorded in the absence of binding partner for Ras by fitting the fluorescence decay to a first order exponential. R_0 and E_0 are the concentrations of Ras and effector respectively.

2.4 Molecular Dynamics Simulations

2.4.1 *Rasβ*

An *in silico* model of Rasβ was constructed using methods described Ensign *et al*.[22,31] This model contained the 5 N-terminal residues (GAMGS) that are not shown in the crystal structure 1LFD[27] but are present on the Rasβ construct after cleavage of the histidine affinity tag during protein purification. This model also contained the WT residue Glu31 instead of Lys31, which was used to crystallize Ras with Ral in crystal structure 1LFD.The mutations K31E, C51A, C80A, and C118A were accomplished using the tleap utility in AMBER tools.[22,32] Finally, nine models containing a single cyanocysteine residue at positions I21, Q25, H27, V29, E31, D33, I36, S39, or Y40 were generated by mutating the appropriate residue to a methionine (which contains the same number of heavy atoms as a cyanocysteine residue) using tleap.[32] The methionine mutation was then subsequently mutated to a cyanocysteine by editing the PDB file. The newly constructed mutants were each subjected to energy minimization by 100 steps of steepest-descents calculation using the GROMACS utility mdrun.[33] The χ_2 torsion around the Cα and Sγ atoms on each cyanocysteinewas rotated in increments of 60˚ for each of the nine mutants. The resulting 54 models were subjugated to further vacuum energy minimization by 100 steps of steepest-descents calculations, and were considered the starting structures of our MD simulations. The 54 energy-minimized structures were placed in a dodecahedral simulation box filled with explicit TIP3P water molecules,[34] sodium ions were added to the box to give the overall model a neutral charge, and the system was subjugated to a final 5000 step steepest-descent energy minimization. The solvent was then allowed to equilibrate for 10,000 2 fs steps by restraining the protein atoms with a harmonic potential of 1000 kJ nm^{-1} mol^{-1} in the three Cartesian

directions.[22,31] After solvent equilibrations, three nanosecond simulations were carried out as discussed previously with two minor exceptions:[22] 1) the simulations were run on the Ranger supercomputer from Texas Advanced Computing Center using a 16 processor distribution; and 2) hydrogen bonds were restrained using the LINCS restraint rather than SHAKE, to allow for multiprocessor calculations.[33] The six χ_2 torsions centered on 0º, 60º, 120º, 180º, 240º, and 300º, and biased with a dihedral restraint potential that was flat within 45º and increased to 1000 kJ mol^{-1} rad^{-2} outside of that range. Each of the six starting torsions was run for three consecutive 1 ns trajectories, resulting in 18 ns of total sampling time for each monomeric Ras construct.

Simulations of each Ras-Ral docked construct were carried out in a similar manner using the molecular models of Ras docked with WT Ral built for a previous study.[22,31] The initial structure for docked simulations was obtained by aligning the Ras construct of interest with the Ras E31K mutant in 1LFD, and aligning WT Ral with the extended N-terminal and C-terminal tails with the Ral structure in 1LFD. Trajectories biased along $\chi_2$were then done as described previously.

The Boltzmann weighted distribution of the χ_2 dihedral for the cyanocysteine was calculated using a weighted histogram analysis method (WHAM) on the full 18 ns trajectories of both the monomer and docked complexes as described earlier.[31] The Boltzmann-weighted probabilities of χ_2 from the final two thirds of simulation (6-18 ns) were compared to the first one third of the simulation (0-6 ns) to confirm that the simulation had converged through this sampling strategy.

2.4.2 *Rafβ*

Models for each Rafβ construct for which experimental data was collected were built starting with the PDB entry 1GUA.[26] Because the protein construct that was crystallized is slightly different from the one used in our experiments, several modifications were made to the protein sequence and structure to get an exact match to our experiments. Seven N-terminal residues (GSHMKTS) that were missing in the crystal structure were taken from three different models to build the missing amino acids into the model protein. First, a TSNT segment was taken from the N-terminus of the PDB entry 3EH1.[35] The NT portion was aligned with the NT of the N-terminus from 1GUA using the align tool in pymol.[36] The duplicate NT segment was deleted, and a new PDB file containing the extra two residues was generated. This model was then converted to a .gro file using the PDB2GMX utility in GROMACS 4.5 using a modified amber 03 force field.[33] The model was subjected to 1 ns of steepest decent energy minimization with potential restraints of 1000 kJ mol^{-1} $radian^{-2}$ placed on all atoms except those on the four N-terminal residues, TSNT. Second, the HMKT sequence was modeled from the near N-terminal segment of PDB entry 2AOT.[37] The C-terminal residue of the segment, T, was aligned with the N-terminal T in pymol[36] and subsequently converted to a .gro file. This new model was then subjected to another 1 ns of steepest decent energy minimization with similar positional restraints on all atoms except those found in the N-terminal sequence HMKTSNT. Finally, the GSH segment was modeled in from the GSH N-terminus of the previously built RalGDS model in a similar fashion to the earlier segments.[22] This final construct was again subjected to another 1 ns of steepest decent energy minimization with positional restraints on all atoms except the N-terminal

GSHMKTSNT atoms. During the energy minimization the potential energy reached -1998.38 kJ/mol, and the largest force on any atoms was 436.09 KJ mol^{-1} nm^{-1} on the backbone carbonyl of residue D81. This result indicates that the newly modeled N-terminal tail did not generate nonphysical steric classes with the crystallized portion of the model.

A Rafβ model containing the complete N-terminus was then made by mutating wild type cysteines at positions 81, 95, and 96 to alanines using the AMBER utility tleap.[32] Each of the nine experimental nitrile probe positions were mutated to cyanocysteins using tleap as described previously.[22,30] The nine models were then energy minimized by 100 steps of steepest decent calculations in vacuum in a continuum dielectric of 78. The χ_2 torsion of the cyanocysteine, the dihedral made from the Cα, Cβ, Sγ, and Cδ atoms of the residue, was then rotated in 60º increments starting from a dihedral angle of 0º by editing the .gro file. This resulted in six different starting structures for each of the nine mutants for a total of 54 Rafβ models. Each of these 54 models were then subjected to another 100 steps of steepest decent energy minimization in vacuum, and the results were considered to be the starting structures for molecular dynamics simulations.

Each of these starting structures were placed in a 12 nm dodecahedral box filled with TIP3P water molecules[34] and counter ion chlorines using the GROMACS utilities genbox and genion respectively.[33] The system was subjected to another 5000 steps of energy minimization by steepest decent simulation. Finally harmonic position restraints of 1000 kJ nm^{-1} mol^{-1} in the three Cartesian directions were placed on all protein atoms,

and solvent equilibration was carried out by 1 ns of simulation. Each of the 54 structures were then subjected to 3 ns of simulation with appropriate positional restraints on the χ_2 dihedral as described before.[22,30-31] Each of the nine mutants had six torsionally biased starting structures sampled for 3 ns, for a total of 18 ns of advanced umbrella sampling simulation time for each nitrile mutant. A snapshot of the simulation was saved every five picoseconds giving a total of 3600 snapshots for each nitrile mutant.

Currently there is no solved crystal structure of the docked complex between Ras and Raf. The simulation model was built by using the PDB file 1GUA containing the GTPase Rap1A bound to Raf, a docked WT Ras model previously built from PDB file 1LFD, and the Rafβ models described earlier.[26-27] The two GTPases in each of the pdb files are similarly folded with a RMSD of 2 Å for backbone atoms.[16,38] The similarities of the GTPases were used to align the docked WT Ras model to the Rap1A found in the PDB entry 1GUA using the align tool in pymol. Similarly the thiocyanate Rafβ models built earlier were individually aligned to the Raf found in PDB entry 1GUA. Finally a PDB containing only the aligned Ras model and aligned thiocyanate Rafβ model was assembled using pymol, and used as the starting point for generating a model for simulation as described earlier. Similarly docked Ralβ – WT Ras models were built by using nine structures generated in a previous study.[27] The nine models chosen to study were Ralβ mutants I18C_{SCN}, R20C_{SCN}, N27C_{SCN}, G28C_{SCN}, N29C_{SCN}, M30C_{SCN}, Y31C_{SCN}, K32C_{SCN}, S33$C_{SCN,}$ and K52C_{SCN}. Energy minimization, solvation, and simulation were carried out as discussed earlier with the Rafβ monomer simulations.

2.4.3 *Ralβ*

Docked Ralβ – WT Ras models were built by using nine structures generated in a previous study described by Ensign *et al*.[27] The nine models chosen to study were Ralβ mutants I18C_{SCN}, R20C_{SCN}, N27C_{SCN}, G28C_{SCN}, N29C_{SCN}, M30C_{SCN}, Y31C_{SCN}, K32C_{SCN}, S33$C_{SCN,}$ and K52C_{SCN}. Energy minimization, solvation, and simulation were carried out as discussed earlier with the Rafβ docked simulations with the exception of Ralβ is the effector modeled at the interface in place of Rafβ.

2.4.3 *RasQ61X*

A model for WT Ras docked with the cyanocysteine-containing downstream effector Ralβ I18C_{SCN} was constructed as described previously.[39] To this model, we generated fifteen mutations to position 61 of Ras; mutations to alanine and glycine were skipped because they lack a χ_1 angle, and cysteine and proline were skipped because of the lack of experimental data. These mutations were made using the tleap utility in AMBER tools using a ffamber03 force field [40] with a parameterized cyanocysteine residue as discussed previously [39,41]. This generated 16 structures of each Ras Q61X mutants (including WT Ras) docked with Ralβ I18C_{SCN}.

Each of the models where then subjected to initial vacuum energy minimizations, using 100 steps of steepest decent integration in the GROMACS utility mdrun [42]. These energy minimized structures were then subjected to torsional biasing by generating six rotomer models 60º apart about the χ_1 dihedral angle (N-Cα-Cβ-Rγ) for each reside at position 61 of Ras. Each of these torsions were sampled using dihedral restraints centered about the angle of interest, flat within 45˚, and with a quadratic force constant of 1,000 kJ mol^{-1} $radian^{-2}$ outside of that range. This generated a total of 6 structures for each Ras

Q61X mutatant. Each of these structures were solvated with tip3p water.[43] Charge neutralization with sodium ions, solvent equilibration, and molecular dynamics sampling were conducted as described previously.[39,41] Three 1 ns trajectories were generated for each rotomer using the mdrun utility in GROMACS for a total sampling time of 18 ns per construct. The Boltzmann weighted torsional distributions for the χ_1 dihedral for position 61 of Ras were calculated using a weighted histogram analysis method (WHAM).[44-45] The torsional distribution of the side chain for the last 12 ns of simulation time was compared to that compiled from the first 6 ns and showed essentially identical WHAM-derived probabilities for side chain distribution, indicating that the simulation had fully converged.

The solvent accessible surface area (SASA) for each sampled residue at Ras position 61 was calculated using the g_sas utility found in GROMACS on each of the trajectories generated during the molecular dynamics sampling. The output was then Boltzmann weighted using the torsional distributions calculated earlier. SASAs were calculated using either the entire residue (including backbone atoms), only side chain atoms, or only atoms that can participate in hydrogen bonding for either the entire residue or the side chain only. In the following discussion, the atoms that can participate in hydrogen bonding (oxygen, nitrogen, and hydrogen atoms bonded to them) are referred to as polar atoms.

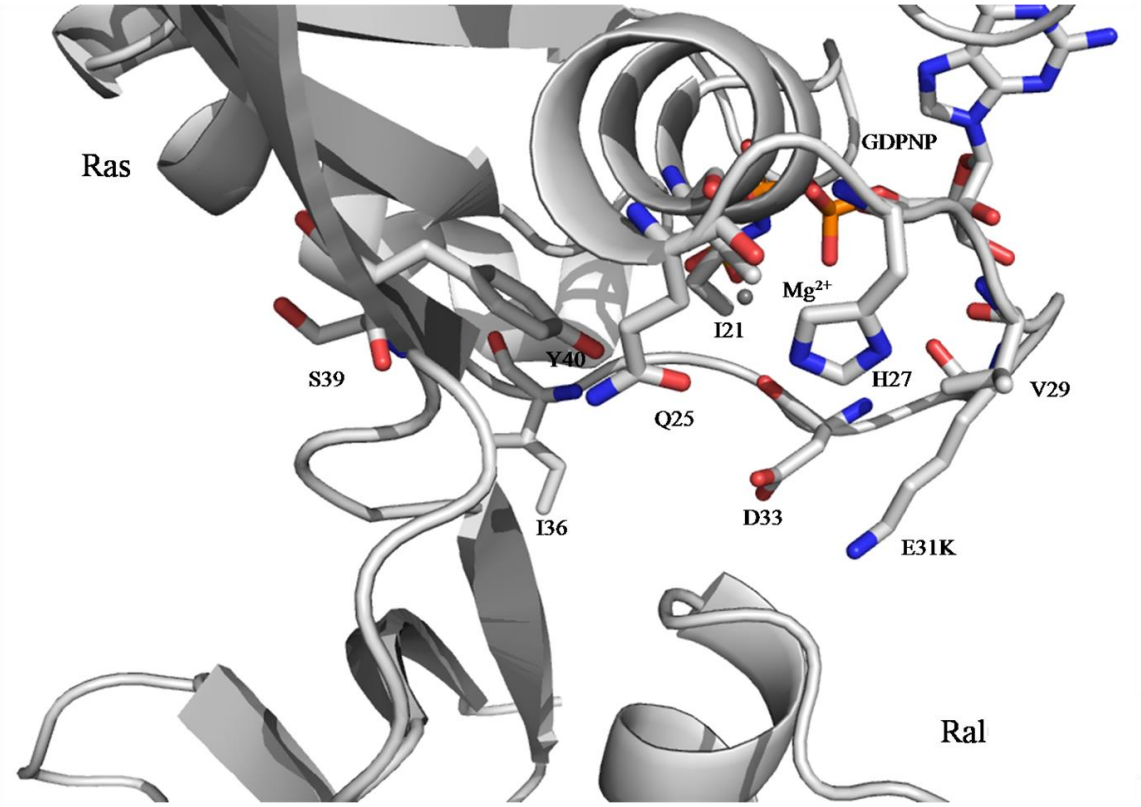

Figure 2-1 Stark probe locations on the Ras surface

Structure of Ras docked with the RBD of Ral from crystal structure 1LFD,[27] identifying the positions of nine residues at the surface of Ras that were selected for mutagenesis and investigation by VSE spectroscopy and MD sampling. Also shown are GDPNP and Mg^{2+} in the active site of Ras.

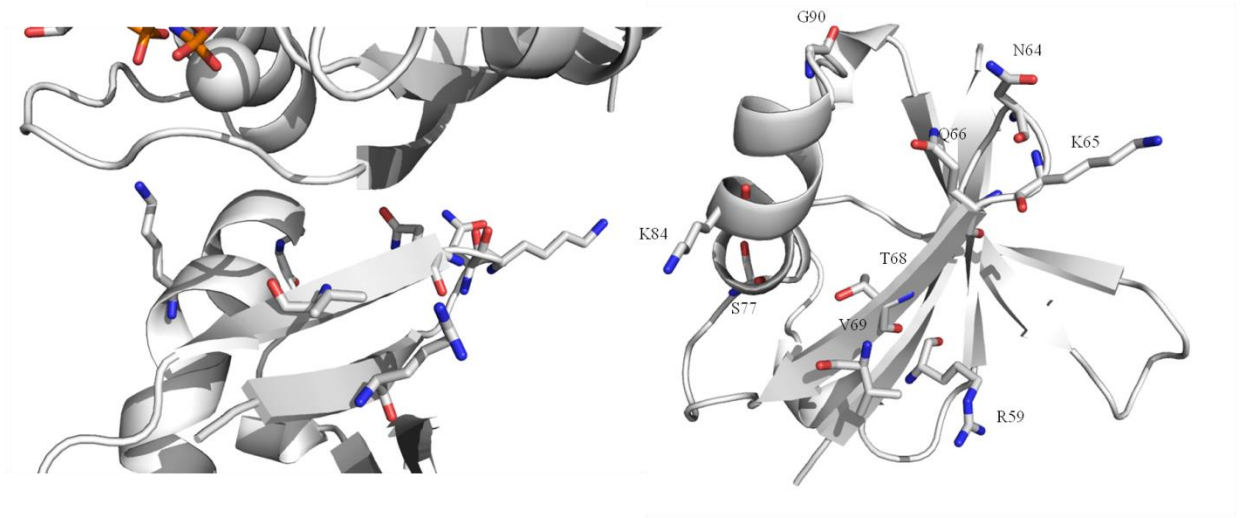

Figure 2-2 Probe locations on Raf's surface
Left: Representation of the modeled binding interface of Ras (top) and Raf (bottom). Right: Ras interacting domain of Raf is shown in a top down view with the nine probe locations used in VSE experiments and MD simulations highlighted as stick models.

Chapter 3 Complementary Electrostatic Fields Created by Protein-Protein Binding at the Interface of Ras and Ral

3.1 Introduction

For some time there has been significant interest in understanding how Ras can differentiate between each of its downstream effectors.[13,16,27] Investigations on this subject have largely been focused on the use of x-ray crystallography to quantify the differences in hydrogen bonds, salt bridges, and hydrophobic interactions between each Ras – effector complex.[26-27,38] Previously work in the Webb laboratory has reported VSE investigations at the GTPase – Ral interface, looking for electrostatic field contributions to the differences in the Ras – Ral complex *versus* the Rap – Ral complex.[22,46] The work presented here once again investigates the protein-protein interface at the Ras – Ral complex from an alternative perspective, the GTPase Ras, through a combination of VSE and computational modeling. Mutations were made to nine residues on the surface of Ras that become immersed in the interface formed between Ras and Ral in the docked complex. The amino acids selected for placement of the nitrile vibrational probe at the Ras-Ral interface are shown in Figure 2-1. Each of these amino acids was mutated to cysteine, then reacted to form the thiocyanate side chain. The absorption energy of each nitrile probe was measured on monomeric Ras. The nitrile-labeled Ras was then incubated with WT Ral, and changes in the absorption energy of each nitrile were measured through Fourier transform infrared (FTIR) spectroscopy. Enhanced molecular

Chapter 3 is based on work previously published.
Walker, D. M.; Hayes, E. C.; Webb, L. J. *Phys Chem Chem Phys* **2013**, *15*, 12241.
Lauren Webb supervised the work. Ellen Hayes was an undergraduate who performed experiments under my supervision.

dynamics simulations employing an umbrella sampling strategy were conducted on both the monomeric (nitrile-labeled Ras) and docked (nitrile-labeled Ras plus Ral) complexes to obtain a Boltzmann-weighted distribution of nitrile probe positions and orientations on each experimental construct. These molecular dynamics simulations were used to interpret how structural changes in the location and orientation of the thiocyanate vibrational probe influenced absorption energy measurements. Finally, these data were compared to a previously published and complementary study of electrostatic fields measured from the Ral side of the Ras-Ral docked complex.[22] These experimental data provide new insight into the role that electrostatic fields play at stable protein-protein interfaces.

3.2 Results

3.2.1 *Dissociation Constant of Ras Constructs With WT Ral.*

Assessing the extent of changes induced into the system through mutation and chemical labeling is necessary to understand the perturbations to the Ras-Ral docking that might occur due to the experimentally introduced thiocyanate vibrational probe. To address this, dissociation constants, K_d, for each of the nine SCN-labeled Rasβ mutants docking with WT Ral were measured and compared to the value for WT Ras (3.5 ± 0.3μM). These results are given in Table 3-1, and show that with the exception of RasE31C_{SCN} and D33C_{SCN}, the presence of the thiocyanate probe causes essentially no deviation in the extent of Ras – Ral interaction compared to the WT system. Ras D33 has been shown to be important for determining docking specificity between Ras and Ral *in vitro* by participating in an extended hydrogen bonding network that stabilizes the

formation of the protein-protein complex, and so it is not unreasonable for the Ras $D33C_{SCN}$ mutation to cause the observed 5-fold increase in K_d.[21,26-27] The sensitivity of the K_d to mutations at Ras E31 is somewhat more surprising. An unrelated GTPase, WT Rap, contains a lysine at position 31, and binds to WT Ral with a K_d approximately an order of magnitude lower than the interaction between WT Ral and WT Ras. It has been previously shown that the mutation Rap K31E converts both the kinetics and electrostatics of binding between GTPase and Ral to the behavior of WT Ras.[46] By analogy, mutation of Rap E31 to an uncharged cysteine mutation should remove unfavorable electrostatic repulsions from this region of the interface and promote the docking interaction. This hypothesis should be explained with a comprehensive analysis of all VSE data available at the Ras-Ral interface, and so will return to this observation below. However, even with these complications, the increase in K_d caused by placing the thiocyanate probe at these locations was less than a factor of 5 even in the most perturbed case, indicating that binding was not abolished between the two proteins, and that in a steady-state experiment at least approximately 96% of the sample remained in the docked configuration. The kinetic data are thus strong experimental evidence that introduction of the small thiocyanate probe does not significantly alter the protein-protein interface under investigation, and that the spectroscopic measurements are being conducted on a system that is substantially representative of the WT interactions.[47]

3.2.2 *Simulations of the Thiocyanate Probe on the Surface of Rasβ.*

Stable protein-protein interactions are formed from the interplay of two main factors: structural complementarity, which includes hydrogen bonding, salt bridge

formation, and hydrophobic effects; and electrostatic fields. To study in detail the role that electrostatics plays in protein-protein interactions, a VSE probe was placed at nine positions on Ras at the interface formed between Ras and Ral described by the 2.1 Å resolution crystallographic structure of Ras E31K bound to WT Ral.[27] Since the effect of a local electrostatic field on the absorption energy of the vibrational probe is proportional to the projection of the field vector onto the nitrile bond axis, in order to interpret vibrational absorption data as an electrostatic field it is necessary to estimate the average orientation of the VSE probe with respect to the binding interface. Therefore molecular dynamics simulations employing an umbrella sampling strategy were used to determine the Boltzmann-weighted torsional distribution of the χ_2 angles for the cyanocysteine side chain on both the SCN-labeled Rasβ monomers and in the docked Rasβ-Ral complex. Probability distributions for the χ_2 angle of the cyanocysteine on each SCN-labeled Rasβ mutant in both monomeric (red) and docked (blue) configurations are shown in Figure 3-1. Each of the nine sampled thiocyanate torsions have probability maxima at approximately ±60˚, ±120˚, and ±180˚, and are thus predictably alkane. (Probability maxima that appear at ±30˚ are most likely artifacts of the torsional biasing during MD simulation, which employed a 30˚-wide flat well for umbrella sampling). There was observed little change in the χ_2 distribution between monomeric and docked SCN-labeled Rasβ complexes, and in no case did formation of the protein-protein interface cause significant distortion of the alkane-like nature of the cyanocysteine side chain. Dihedral angle probability distributions were determined for the first 6 ns and were compared to the probability distributions determined during the last 12 ns of simulation. There was no

significant difference between these two distributions, suggesting that the simulations had achieved convergence for the dihedral orientation and have generated a Boltzmann-weighted statistical ensemble of the most probable orientations of the nitrile with respect to the χ_2 dihedral angle of the cyanocysteine side chain. These Boltzmann-weighted probability distributions then become the basis for calculating Boltzmann-weighted averages of other spatially relevant attributes of the thiocyanate probe in three-dimensional space.

Using these statistical ensembles of thiocyanate orientations, the orientation of the thiocyanate with respect to the protein-protein interface based on an azimuthal (ϕ) and polar (θ) angle polar coordinate were measured.[22] The azimuthal angle was defined as the angle of elevation of the VSE probe with respect to a plane formed at the binding interface, shown schematically in Figure 3-3, where the SCN-labeled Rasβ mutant is located above the surface plane (i.e. the $\phi = 0^\circ$ axis), while Ral is below the surface plane. Results for both the monomer (red) and docked (blue) SCN-labeled Rasβ-WT Ral complexes are given in Figure 3-3. In all cases, the probe pointed outward to the solvent on the monomer, and in most cases remained in this orientation upon binding to WT Ral. However, mutants Rasβ $D33C_{SCN}$ and Rasβ $S39C_{SCN}$ both show a preferential shift away from Ral and towards the interior of Rasβ upon docking with WT Ral. By examining representative snapshots along our sampling trajectory, it was apparent that the change in Rasβ $S39C_{SCN}$ azimuthal angle upon docking was caused by the steric clashes between the thiocyanate and the bulky side chain of Ral Y28 that is introduced upon docking. This

resulted in a change of 60˚ in the χ_1 angle for the thiocyanate to point upwards into the interior of Ras. The cause for the change in Rasβ $D33C_{SCN}$ orientation appeared to be from the flexibility of the so-called "switch I" loop (residues 31-40) that has a small but significant structural difference between the monomer and the docked complex (measured as a RMSD of 0.48 Å in X-ray structures comparing monomeric and docked states).[27] This was replicated in an observed RMSD of approximately 0.5 Å in this region during the simulation when comparing the Cα backbone atoms for monomer and docked complexes, and indeed, the calculated variance for the cyanocysteiene side chain (shaded regions in Figure 3-3) was largest at Rasβ $D33C_{SCN}$ compared to other probe locations. However, in general, variance for each azimuthal angles on both monomeric and docked complexes remained quite low (<±13˚), did not display any systematic behavior, and do not appear to be correlated in any way with vibrational absorption energy of the thiocyanate, discussed below.

Another measure of the position of the SCN probe with respect to the protein surface is given by the thiocyanate's solvent accessible surface area (SASA), a measure of how much of the probe is exposed to water based on its orientation at the protein surface. The SASA for the entire cyanocysteine residue was calculated from the Boltzmann-weighted ensemble of structures for both monomeric and docked complexes using the Gromacs utility g_sas, and are given in Table 3-2.[33] These residues were chosen for our studies because of their solvent-accessible location on the binding interface of Rasβ, and SASA values as high as 140$Å^2$ were measured for similarly placed solvent-accessible nitrile probes in other protein constructs in our laboratory.[22] However, the

SASA values measured were relatively small, 20 to 60 $Å^2$, and did not decrease significantly upon docking with WT Ral. These results indicate that most residues are being excluded from water on the surface of the Rasβ monomer because of their orientation with respect to the protein surface. This is not surprising when considering the measured azimuthal angles shown in Figure 3-3, which demonstrated that most cyanocysteine mutants lie nearly parallel to the interface in both the monomeric and docked complexes. Taken as a whole, these low measured SASA values for each mutant suggest that differences in absorption energies of the monomer are derived from electrostatic fields being generated by the protein itself rather than being dominated by interactions with water such as hydrogen bonding.[22,31,48-49]

A second metric of the orientation of the thiocyanate probe with respect to the Rasβ-Ral interface was the angle of rotation of the probe about an axis orthogonal to the binding interface; we refer to this angle as the polar angle, θ, which is described in Figure 3-6. This angle represents the degree of conformational variability of the probe with respect to the center of mass of the protein and parallel to the binding interface. Because the position of the residue with respect to the center of mass is different for each nitrile location, Figure 3-4 is given to aid in visual interpretation of results for the polar angle. When the cross-hairs of the axes shown in Figure 3-5 are translated to the center of each spherical Cα atom they become the origin for θ. These results are shown in Figure 3-5 for both monomeric (red) and docked (blue) complexes. The measured value of θ varied considerably depending on the location of the cyanocysteine mutant with respect to the

center of mass of the protein, and therefore on its location around the protein interface. Although there was a greater variability in this measurement between the monomeric and docked complexes than seen for χ_2 torsional angles or azimuthal angles (measured as a variance and shown as the shaded regions on Figure 3-6), at only one position, Rasβ H27C_{SCN}, did protein-protein docking cause the cyanocysteine side chain to assume a significantly different orientation. Careful examination of representative snapshots taken during the MD trajectory indicate that this change of ~130˚ between the monomeric and docked complexes was caused by a steric clash between the thiocyanate and the bulky side chain of WT Ral L52, forcing the χ_2 orientation of H27$C_{SCN}$to rotate approximately 40º from its position in the Ras monomer. This small dihedral change, which did not disrupt the alkane-like nature of the side chain, is magnified when viewed relative to the polar axis that is orthogonal to the surface plane, which is the value measured by θ. The result is a large shift if the polar angle of the thiocyanate upon docking. In no case was the variance in θ correlated with vibrational absorption energies of the thiocyanate probes, discussed below.

3.2.3 *Vibrational Stark Effect Spectroscopy.*

Investigations of the binding interface are shown in Table 3-3 and in Figures 3-6 and 3-7. Figure 3-6 is a representative of the two normalized vibrational spectra of Rasβ I36C_{SCN} monomer and docked with Ral. Two prominent features of the spectrum is the quite red shift associated with docking the I36C_{SCN} mutant to WT Ral, along with the slight narrowing of the peak width. The uniform Gaussian symmetry and narrowing of the docked complex spectra do indicate the observation of a steady-state interaction

between the two proteins. The low variance in both ϕ (Figure 3-3) and θ (Figure 3-5) confirm that this cyanocysteine populates one configuration in the monomeric protein and that its orientation in the complex does not change significantly upon docking with WT Ral. The absorption energy of the thiocyanate probe on all monomeric Rasβ constructs, shown in Figure 3-8A and reported in Table 3-3, varied over 4 cm^{-1} (2159.0 – 2162.9 cm^{-1}); each individual position was measured to a standard deviation of at least < 0.6 cm^{-1} and usually smaller. Taken together with the SASA results discussed above, this suggests that although all of these probes are on the surface of the protein of the Rasβ monomer, these thiocyanates are relatively sequestered from solvent by the surface of the protein.[22]

The experimentally measured the absorption energy of the nitrile frequency in methyl thiocyanate (MeSCN) was found to be 2162.1 ± 0.1 cm^{-1} in the experimental buffer containing 10% glycerol. This represents the absorption of the nitrile under fully solvent-exposed conditions, when the nitrile is mostly likely acting as a hydrogen bond acceptor from the solvent.[50-51] Because of convolutions of hydrogen bonding and electrostatic effects, this is therefore a complication when attempting to interpret vibrational absorption energy.[49] The fact that 8 of the 9 cyanocysteine mutants studied here had absorption energies less than the absorption energy of MeSCN is further evidence that these probes are not interacting with water to any great extent. The one exception to this observation, Rasβ $I36C_{SCN}$, with an absorption energy in the monomeric form of 2162.9 ± 0.4 cm^{-1}, also showed the largest decrease in SASA going from the monomeric to docked complexes, 40 $Å^2$ and 25 $Å^2$, respectively. This is expected if the

side chain is exposed to water that is then displaced when the protein-protein complex is formed. The vibrational absorption results and MD simulations thus both support the conclusion that with the possible exception of Rasβ I36C_{SCN}, these nitrile probes are not participating in extensive hydrogen bonding interactions with water in either the monomeric or docked complexes, and that therefore they are useful probe positions for investigating the magnitude and function of electrostatic fields at the Ras-Ral interface.

After the absorption energy of the SCN-labeled Rasβ monomer was measured, the protein was then incubated with WT Ral and the absorption energy of the thiocyanate was measured in the docked complex. The results showing the change in absorption energy between the monomeric and docked complexes, $\Delta\nu_{obs}$, are described in Table 3-3 and Figure 3-7B. Six of the nine mutants experienced a lower absorption energy in the docked complex *versus* the monomer, while the remaining three experienced an increase in absorption energy. The change in absorption energy ranged from -2.8 ± 0.4 cm^{-1} to +0.9 ± 0.4 cm^{-1}, representing a change in electrostatic field of over 5 MV/cm (+4.0 to -1.3 MV/cm, equation 1) depending on the location of the nitrile probe. Interestingly, two of the three mutant locations that experienced an increase in absorption energy upon docking, Rasβ D33C_{SCN} and Rasβ S39C_{SCN}, were the only two mutants to experience a large change in the azimuthal angle, ϕ, from the monomeric to docked complexes. In both cases, the cyanocysteine side chains at these locations moved from relatively near the surface of the Rasβ protein to above the Rasβ-Ral surface plane, showing that these side chains were sequestered inside the Ras-side of the interfacial area formed by the

docked complex. The full width at half maximum (fwhm) for each of the peaks decreased upon effector binding for each probe, sometimes significantly (~-1.0 cm^{-1} for 7 if 9 of the studied mutants), but this was not correlated to K_d measurements or MD sampling in any way.

3.3 Discussion

If electrostatic fields are an important mechanism for the formation and function of stable and specific protein-protein interactions, then docking partners will have to recognize each other through a pattern of weak but long-range electric fields across the docking surface. When rationalizing the structure of docked complexes, many researchers point to the apparent matching of complementary electrostatic fields to justify why a single thermodynamic orientation is selected over a large number of possibilities.[52] The surface area of the Ras-Ral interface is approximately 1500 $Å^2$; systematically probing the electrostatic environment along this large interface allows us to test whether selecting for electrostatic complementarity is a plausible mechanism for orienting the two proteins into their observed configuration in the docked complex. The study reported here, employing nine nitrile probes along the Rasβ-Ral interface, is complementary to a previously published report in which nine thiocyanate probes were placed along the Ral surface, then docked with WT Ras.[22] The present results can therefore be combined with published data to create a global perspective of the role of electrostatic fields in this specific docking interaction.

Now that both sides of the Ras – Ral complex have been investigated, it is instructive to compare results from thiocyanate probes introduced from two different

proteins but sitting at the same position of the protein-protein interface and interacting with residues from the other protein. This is most easily seen when the direction of the energy shift of the thiocyanate absorption (higher or lower energy) *versus* the absorption energy in buffer is superimposed on the structure of the docked complex itself. In Figure 3-9, positions of the protein surface where the nitrile probe experienced $\Delta\nu_{obs} < 0$ are shown in red, while positions that resulted in $\Delta\nu_{obs} > 0$ are shown in blue, compiled both from the data in Table 3-3 and the data in Table 3-2 of Stafford, *et al.*[22] In Figure 3-8A, this interface is shown side-on, where transparent red surfaces allow us to visualize the blue interior of the interface. In Figure 3-8B, the interface has been opened like the pages of a book, and these same data are shown looking onto the protein surfaces in the formed interface. This comprehensive data set, describing a large number of individual experiments of a nitrile probe moved systematically with Ångstrom resolution around the protein-protein interface, shows a distinct pattern of interacting residues based on their position in the protein-protein complex. Thiocyanate probes on the surface of Rasβ demonstrated a distinct pocket in which the thiocyanate absorption energy shifted to higher energy, defined by the residues D33C_{SCN}, S39C_{SCN}, and Y40C_{SCN}. This pocket surrounds Ralβ K32C_{SCN}, which also experiences a blue shift moving from the monomeric to docked complexes. This pocket of $\Delta\nu_{obs} > 0$ (and thus $\Delta\vec{F}_{protein} < 0$) is completely surrounded by a ring of residues that all had measured$\Delta\nu_{obs} < 0$ (and thus $\Delta\vec{F}_{protein} > 0$) from both proteins: Rasβ I21C_{SCN}, Q25C_{SCN}, H27C_{SCN}, V29C_{SCN}, E31C_{SCN}, and I36C_{SCN}; and Ralβ I18C_{SCN}, N29C_{SCN}, Y31C_{SCN}, S33C_{SCN}, and N54C_{SCN}. This

appears to create a pocket of electrostatic complementarity (blue) in the middle of a ring of alternate complementarity (red) in the formed Ras-Ral interface. This is exciting evidence that the role of electrostatic fields at this protein-protein interface includes a mechanism for orienting the two proteins in the correct positions for the function of the docked complex.

This complete view of electrostatic fields at the Ras-Ral interface helps explain two key observations, the increase in K_d for the formation of the docked interfaces containing Rasβ $E31C_{SCN}$ and $D33C_{SCN}$, and the curious placement of the positively charged Ral K52 side chain near the Mg^{2+} bound to the Ras active site. Figure 3-9 shows clearly that Ras D33 is crucial for creating the electrostatic pocket that surrounds Ral K32 in the docked structure. This has previously been identified as a hydrogen-bonding interaction,[13,26] and without question that element of the structure contributes to the stability of the structure. However, Ras D33 is necessary to create the extended patch of electrostatic complementarity in the center of the docked interface that recognizes the contribution from Ral K32. Without this noncovalent interaction, the binding between Ras and Ral will become weaker or less specific for the particular structure of Ras and Ral leading to this specific configuration, both of which would cause an increase in the rate of dissociation of the docked complex. This also explains why the docked configuration places the positive charge of Ral K32 so near the Mg^{2+} ion complexed to GPDNP in the active site of Ras. This repulsive Coulombic interaction is mitigated by the pocket of electrostatic potential that has been created by the proximity of Ral K32 to Ras D33, S39, and Y40. Ras E31 appears to serve the same purpose of creating the ring

of high $\Delta\vec{F}_{protein}$ (low $\Delta\nu_{obs}$, red) that surrounds the internal binding pocket. These details only become apparent or relevant once the global electrostatic field around the entire protein-protein interface has been mapped and investigated in its entirety.

In summary, I have presented a system the systematic measurement electrostatic fields along the interface of the human oncoprotein Ras when docked with the RBD of the downstream effector protein Ral. Molecular dynamics simulations demonstrate that the thiocyanate probes deployed along the surface of Ras are on average oriented approximately horizontal to the Ras-Ral interface, and thus are not likely to be engaged in extensive hydrogen bonding with solvent water molecules. When combined with an extensive data set previously obtained for a similar study on the surface of Ral, I have identified regions of electrostatic complementary created by the docked interaction between Ras and Ral that appear to be significantly responsible for creating this docked configuration. It must be emphasized these electrostatic fields can only be measured at positions in which a nitrile probe can be reliably placed, and only in orientations determined by the nitrile vector's orientation in three-dimensional space. Even though the selected SCN-labeled residues are near to or sequestered within the formed protein-protein interface, this does not guarantee that all electrostatic contributions have been found. Electrostatics calculations designed to test this hypothesis further and kinetics experiments to measure the effect of mutations to these residues are underway in our laboratory and will be reported in a future study.

Table 3-1: Binding kinetics of WT Ras and each of the Rasβ mutants docked with WT Ral.

Ras Mutant	K_d (μM)[a]
WT	3.5 ± 0.3
Rasβ I21C_{SCN}	5 ± 1
Rasβ Q25C_{SCN}	4.3 ± 0.4
Rasβ V29C_{SCN}	5.5 ± 0.4
Rasβ H27C_{SCN}	5.5 ± 0.6
Rasβ E31C_{SCN}	12.3 ± 0.2
Rasβ D33C_{SCN}	17±3
Rasβ I36C_{SCN}	4.4 ± 0.2
Rasβ S39C_{SCN}	7.0 ± 0.6
Rasβ Y40C_{SCN}	4.4 ± 0.7

[a]Dissociation constants were obtained by fitting k_{obs} from the GDI assay to equation 2. Errors are reported as one standard deviation of at least three experimental replicates.

Table 3-2: Solvent Accessible Surface Area calculations of both the monomer and docked complex of each Rasβ mutant.[a]

Mutants	Monomer SASA ($Å^2$)	Docked SASA ($Å^2$)
Ras β $I21C_{SCN}$	20 ± 10	30 ± 10
Rasβ $Q25C_{SCN}$	30 ± 10	20 ± 10
Rasβ $H27C_{SCN}$	50 ± 10	40 ± 10
Rasβ $V29C_{SCN}$	60 ± 10	60 ± 10
Rasβ $E31C_{SCN}$	56 ± 9	40 ± 10
Rasβ $D33C_{SCN}$	50 ± 10	50 ±10
Rasβ $I36C_{SCN}$	40 ± 10	25 ± 9
Rasβ $S39C_{SCN}$	50 ± 10	40 ± 10
Rasβ $Y40C_{SCN}$	30 ± 10	15 ± 8

[a]Values calculated from the Boltzmann-weighted statistical ensemble of thiocyanate χ_2 torsion angles. The error reported is one standard deviation obtained from the Boltzmann-weighted conformational sampling.

Table 3-3: Comparison of the vibrational absorption energies of each of the nine SCN-labeled Rasβ mutants in both monomeric and docked complexes.[a]

	Monomer		Docked with WT Ral		
Mutants	ν_{obs} (cm^{-1})	fwhm(cm^{-1})	$\Delta\nu_{obs}$(cm^{-1})	Δfwhm(cm^{-1})	$\Delta\vec{F}_{protein}$ (MV/cm)
Ras β $I21C_{SCN}$	2161.2 ± 0.4	11.6 ± 0.3	-0.42 ± 0.5	-1.0 ± 0.5	0.6
Rasβ $Q25C_{SCN}$	2160.0 ± 0.6	12.0 ± 0.5	-1.2 ± 0.6	-0.8 ± 0.6	1.7
Rasβ $H27C_{SCN}$	2160.5 ± 0.3	11.7 ± 0.6	-1.27 ± 0.9	-1.2 ± 0.9	1.8
Rasβ $V29C_{SCN}$	2161.1 ± 0.1	13.6 ± 0.2	-0.9 ± 0.4	-1.1 ± 0.4	1.3
Rasβ $E31C_{SCN}$	2161.3 ± 0.3	12.4 ± 0.3	-2.8 ± 0.4	-0.4 ± 0.4	4
Rasβ $D33C_{SCN}$	2161.7 ± 0.2	14.3 ± 0.7	0.9 ± 0.4	-0.2 ± 0.6	-1.3
Rasβ $I36C_{SCN}$	2162.9 ± 0.4	11.8 ± 0.3	-1.2 ± 0.5	-1.4 ± 0.5	1.7
Rasβ $S39C_{SCN}$	2160.8 ± 0.4	12.5 ± 0.8	0.6 ± 0.2	-0.7 ± 0.3	-0.9
Rasβ $Y40C_{SCN}$	2159.0 ± 0.2	13.7 ± 0.6	1.0 ± 0.5	- 0.9 ± 0.5	-1.4

[a]The error reported is one standard deviation of at least three experimental replicates.

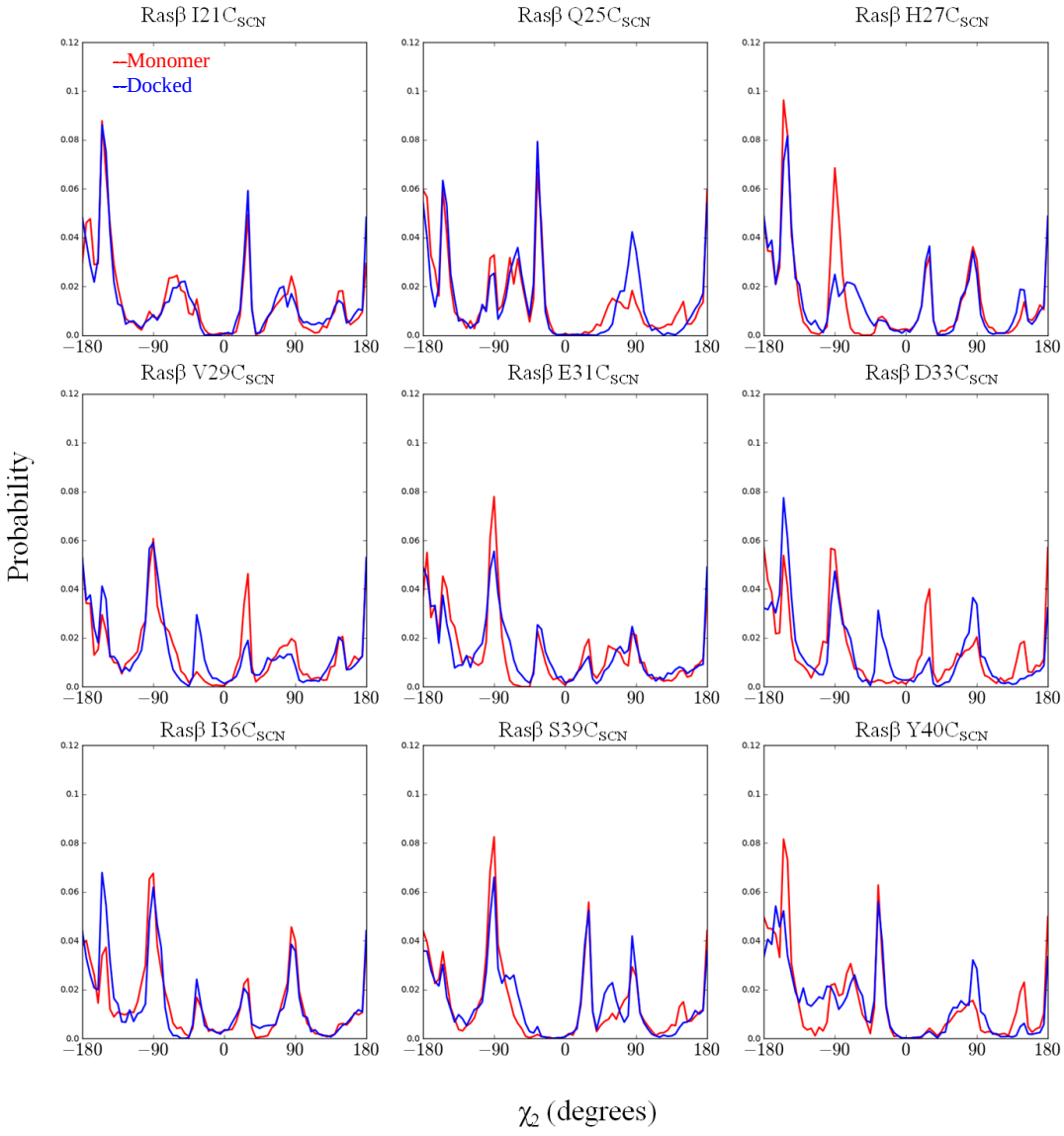

Figure 3-1 Cyanocystein χ_2 torsional distribution

Boltzmann-weighted torsional probability distributions of the χ_2 dihedral of the cyanocysteine for the monomeric Rasβ protein (red), and docked to WT Ral (blue). Each distribution represents 18 ns of sampling at 300 K in explicit TIP3P waters.

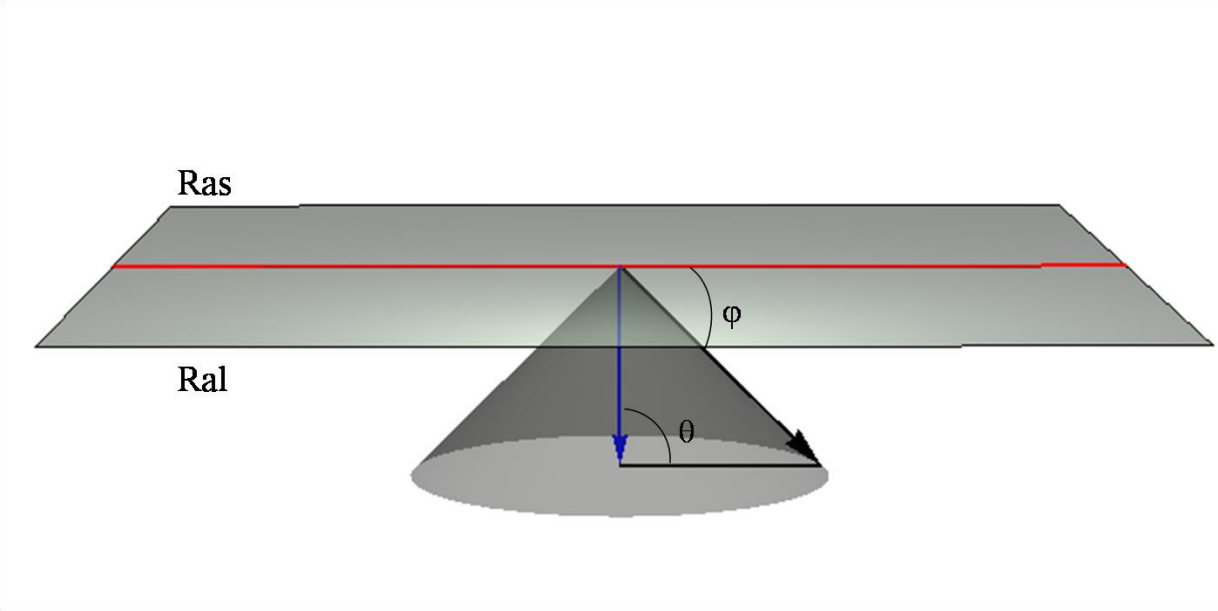

Figure 3-2 Representations of the azimuthal and polar angles

The azimuthal angle, ϕ, is a measurement of the elevation from the binding plane between the proteins. The polar angle, θ, is a measurement of rotation about polar axis depicted as a blue line orthogonal to the binding axis shown in red.

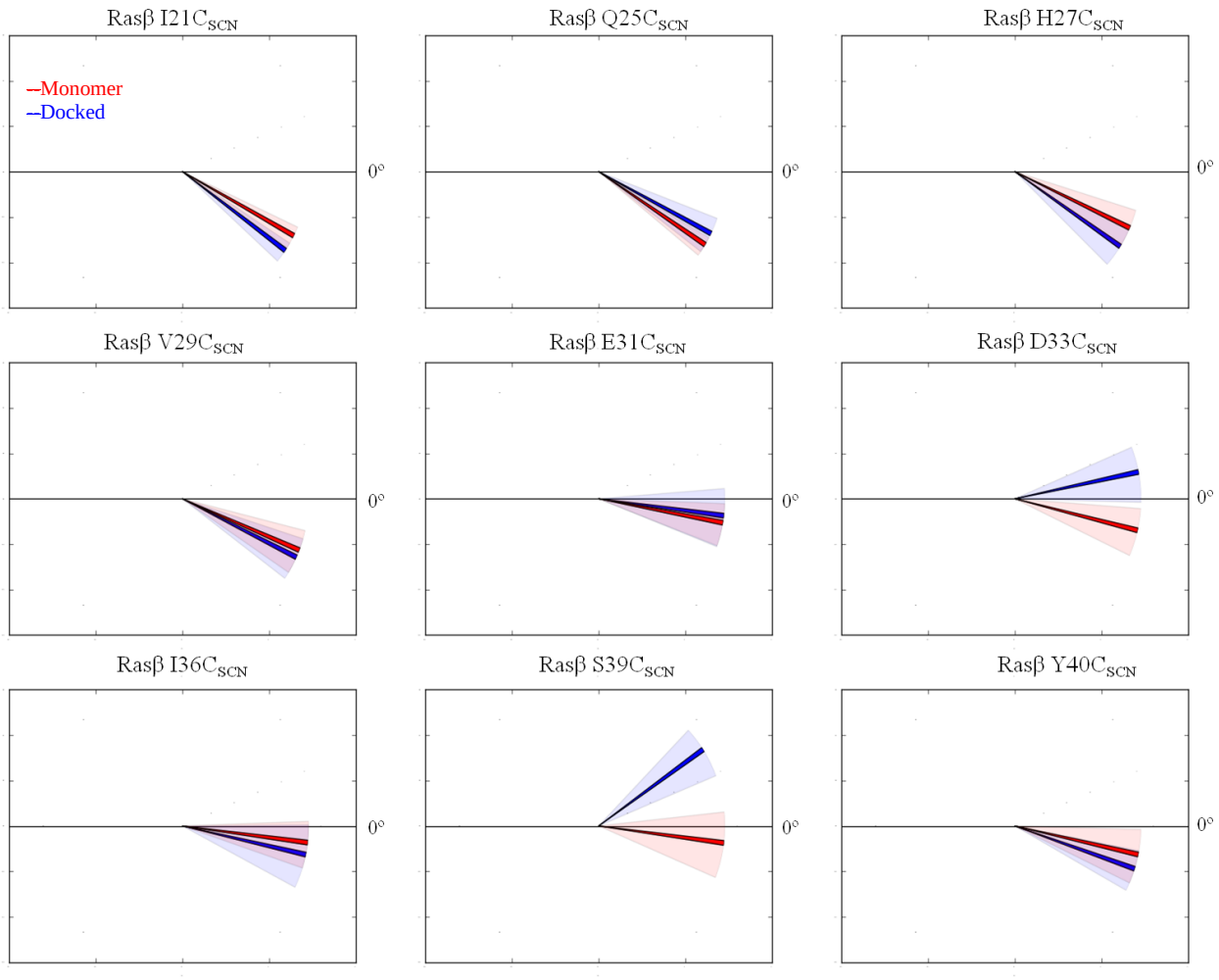

Figure 3-3 Boltzmann-weighted azimuthal angles of the nine probe locations on Rasβ

Boltzmann weighted averages of the azimuthal angle made from the nitrile bond in the thiocyanate to the binding plane between Ras and Ral. The ensemble averages are given as solid lines, with variance about the average shown by the shaded areas. Monomeric sampling is shown in red, and the docked sampling is shown in blue. In this view Ras is situated above the horizontal axis, and Ral is situated below the horizontal axis.

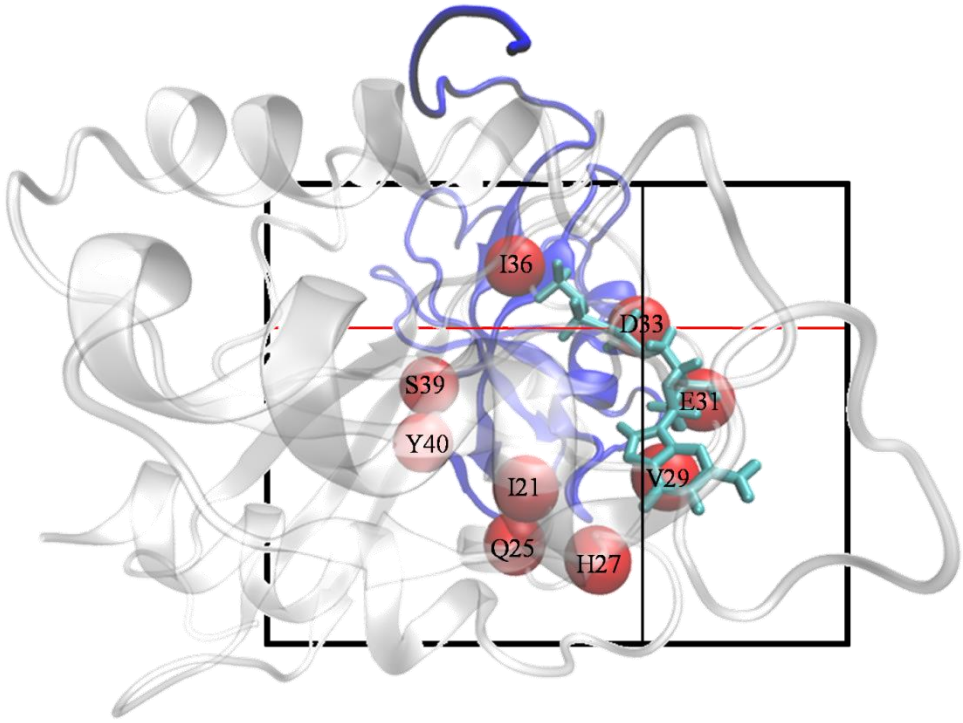

Figure 3-4 Representation of the polar angle for each Rasβ mutant

Ras is shown as transparent white, the Cα atoms of each cyanocysteine residue are shown as red spheres, and Ral is shown in blue. The polar angle can be visualized by translating the axis origin of the crosshairs to the center of each sphere.

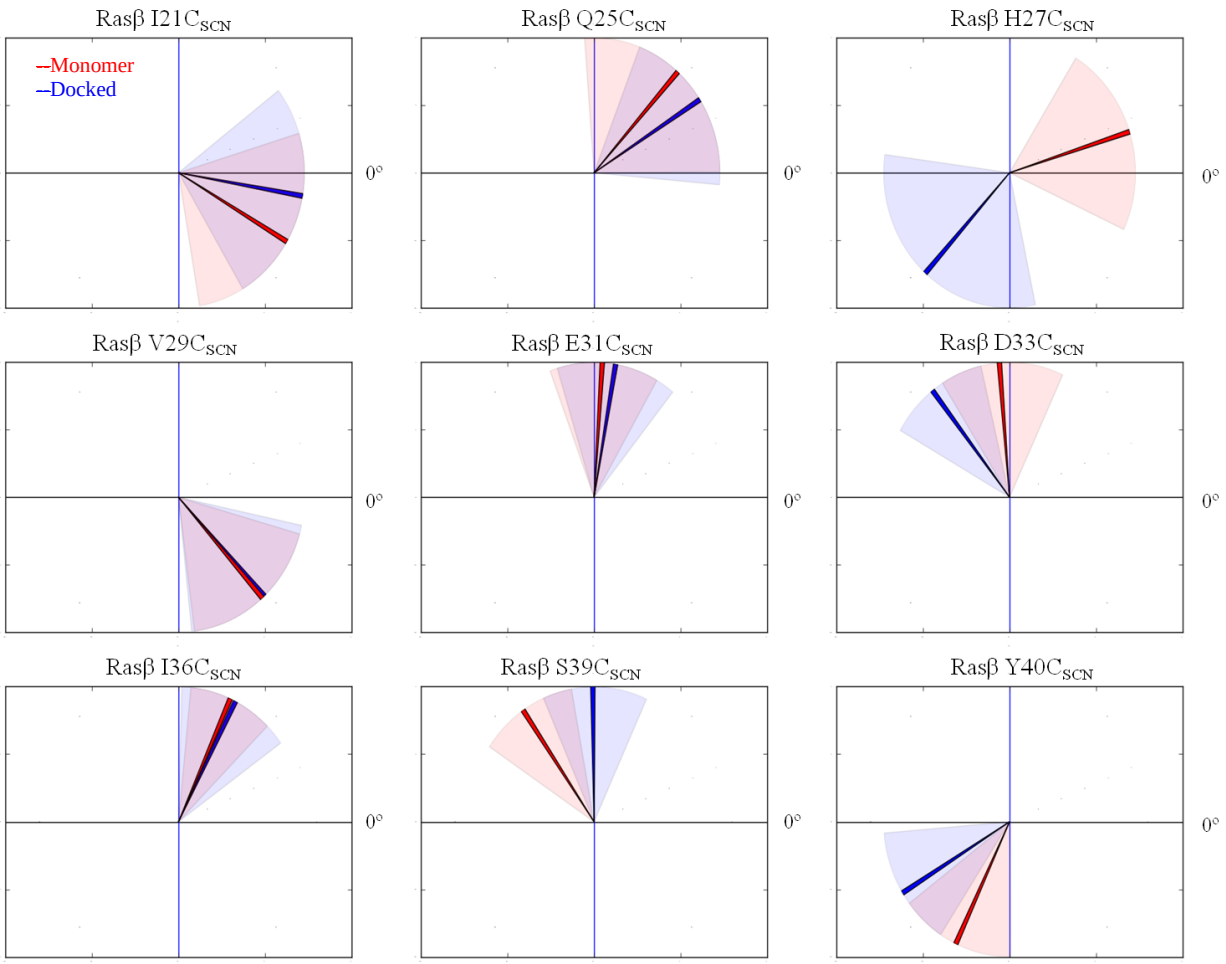

Figure 3-5 Boltzmann-weighted azimuthal angles of the nine probe locations on Rasβ

Boltzmann-weighted averages of the polar angle between Ras and Ral made between the polar axis shown in blue to the nitrile bond in the cyanocysteine side chain. Monomeric sampling is shown in red, and the docked sampling is shown in blue. The ensemble averages are given as solid lines, with variance about the average shown by the shaded areas.

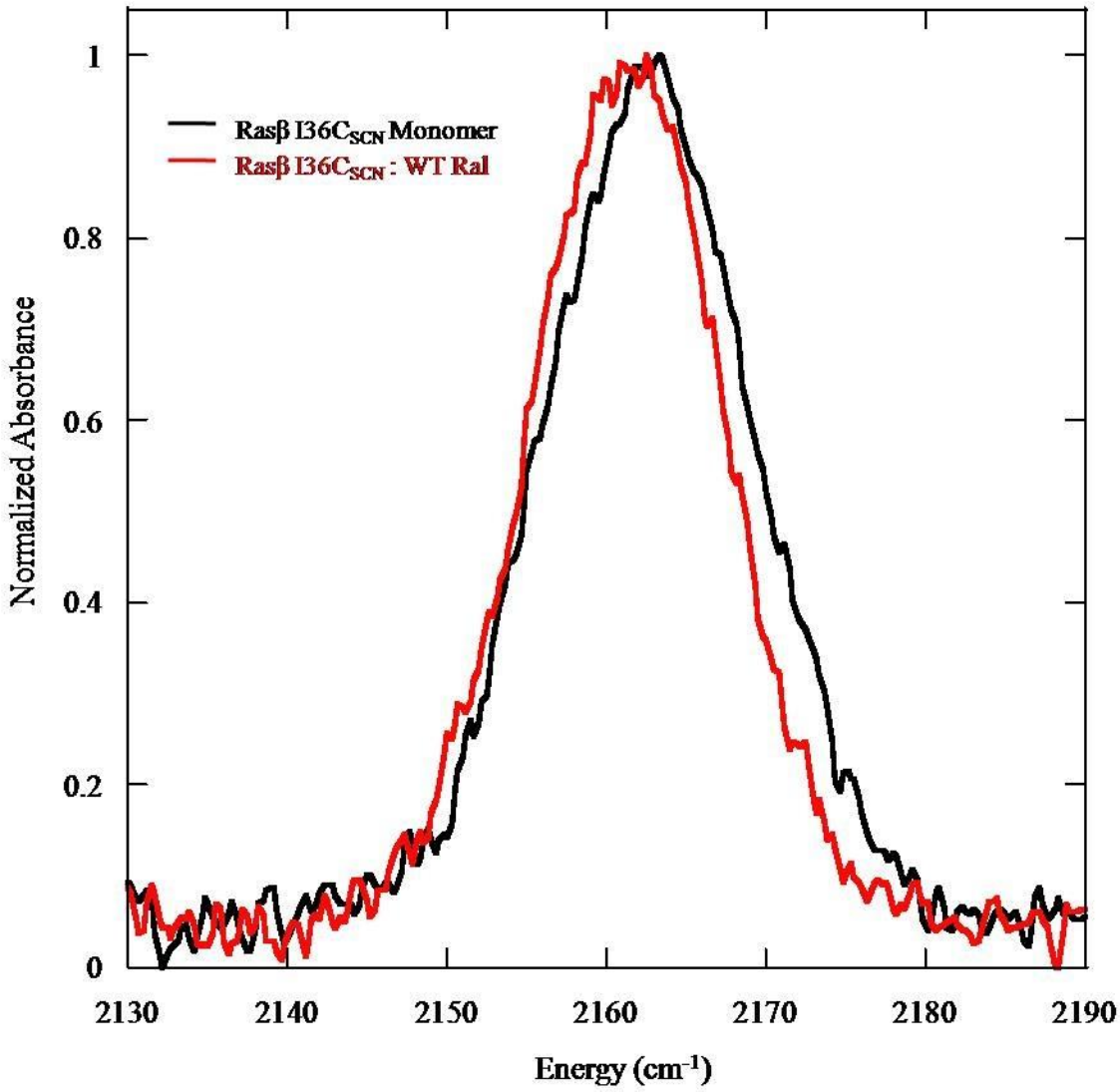

Figure 3-6 Representative Stark effect spectra

Representative spectra of the monomeric RasβI36C$_{SCN}$ (black) and RasβI36C$_{SCN}$ docked with WT Ral (red). The absorption energy of the nitrile at this position decreases by ~ 1 cm^{-1} upon docking with WT Ral compared to the monomeric state.

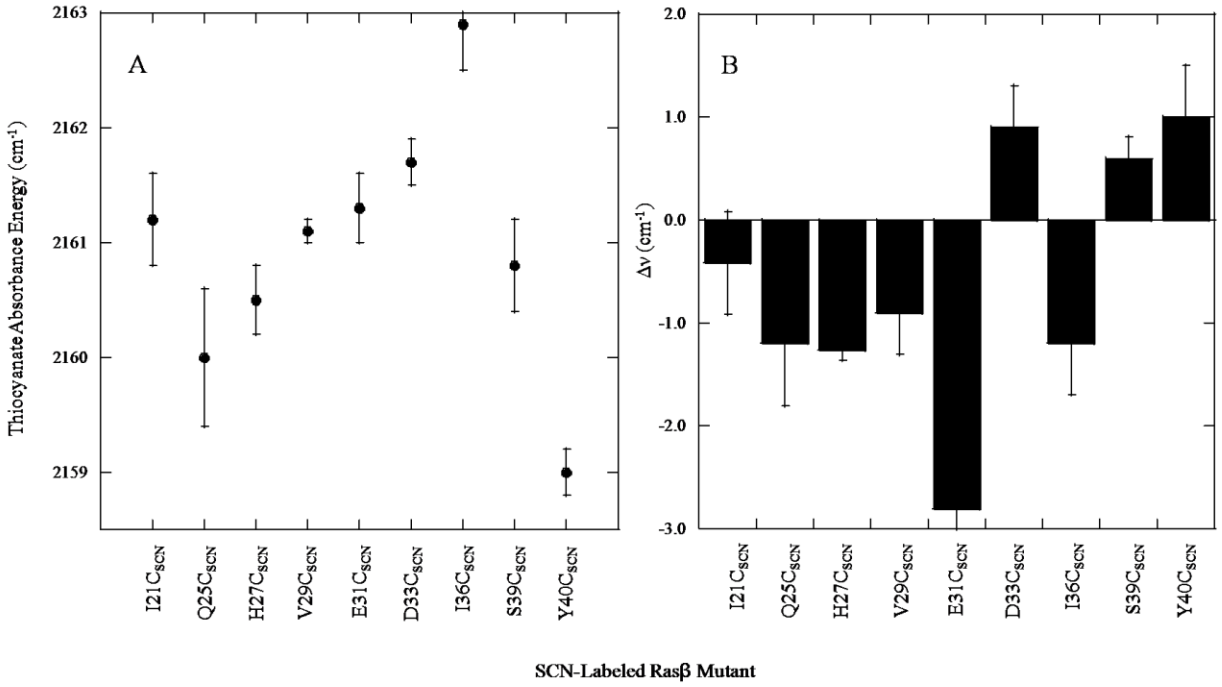

Figure 3-7 Comparison of the nine Rasβ probes docked vs monomer absorption energies

A) Absorption energies of each of the nine monomeric Rasβ probes. B) The measured spectral change to the thiocyanate probe as each Rasβ mutant binds to WT Ral. Each spectra was taken in a solution of 50 mM Tris pH 7.5, 100 mM NaCl, and 10% glycerol.

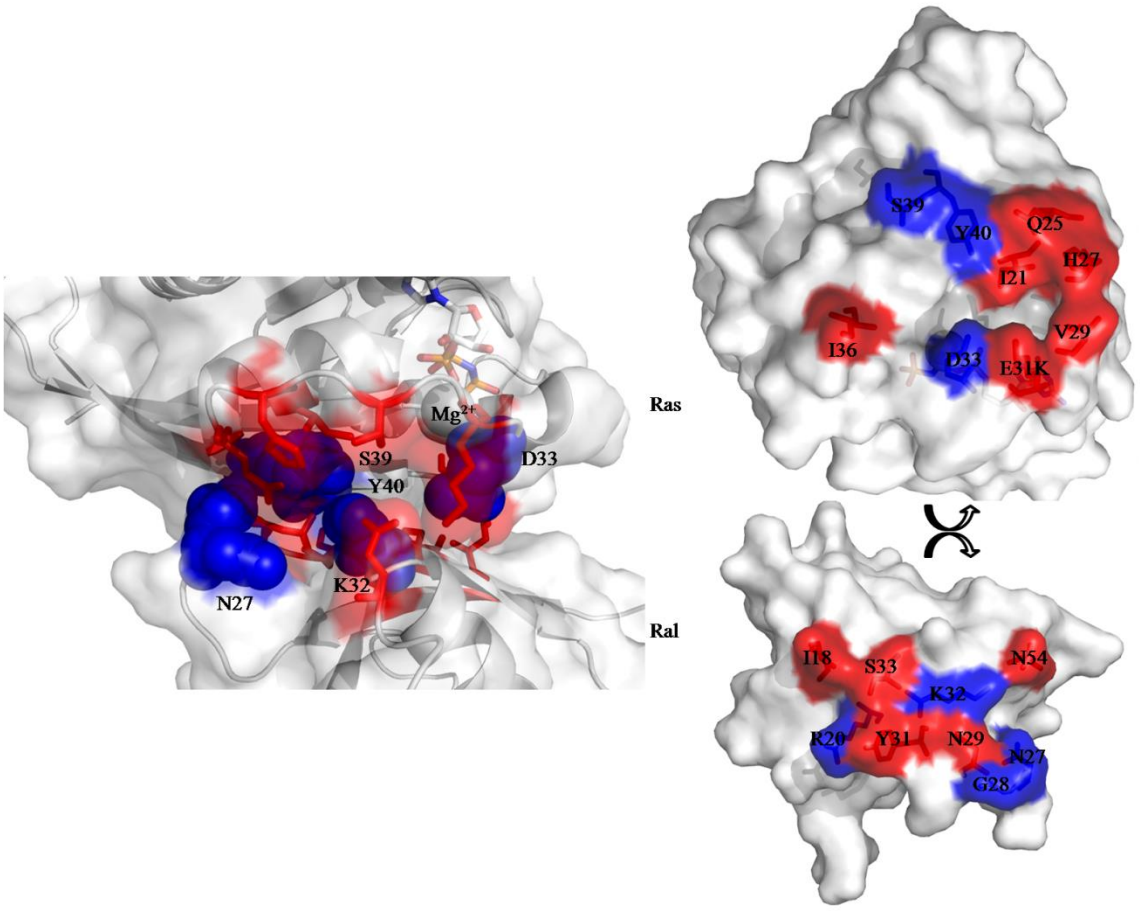

Figure 3-8 Comparison of observed Stark shifts between Ras probes and Ral probes during the formation of the Ras – Ral complex

A: side view of the Ras-Ral interface. The direction of the energy shift of the nitrile at each position is indicated by blue (higher energy) and red (lower energy) labels. Transparent white surfaces represent the exterior of the protein surface. B: view of the interface of Ras (top) and Ral (bottom) to view the position of each residue discussed here. Blue and red labels represent shifts in the nitrile's vibrational frequency upon docking to higher (blue) or lower (red) energy).

Chapter 4 Ras Effector Tilt Angle Differences Between Raf and Ral Explained Through Conserved Electrostatic Fields

4.1 Introduction

One of the striking consequences arising from of a lack of understanding electrostatics fields in protein – protein interactions is that it becomes difficult to rationalize the discrimination exhibited by protein families with binding targets that are homologous in sequence or structure.[14] Ras is a protein in the Ras superfamily of GTPases that has been a subject of intense research for the past two decades due to its involvement in many important signaling cascades.[7-8] Although Ras is nominally a GTPase, like most other signaling proteins its function depends on timely, effective, and proper interactions with many other proteins throughout its catalytic cycle. Interestingly, a few isoforms of this single protein are responsible for a variety of cellular functions ranging from cell division to vesicle transport, depending on its cellular location and which downstream effectors it interacts with in its active, GTP-bound state.[14,18,53] However, *in vitro* studies have shown that Ras can differentiate its binding between downstream effectors independently of location in the cell.[20-21,26] The two most studied downstream effectors, Ral and Raf, have two significantly different binding dissociation constants, K_d, ~1 μM and ~20 nM respectively.[26,46] These two effectors share similar ubuquitin-like folds with a backbone RMSD of 3.6 Å, but have virtually no sequence identity within the Ras binding domain (RBD) of either effector with one another (as determined by BLAST).[16,25,27] Despite their similar folds, crystal structures of the two RBDs bound to structurally identical GTPases show a significant difference in the

orientation of the RBDs when docked to the GTPase. As shown in Figure 1-8, there is a noticeable ~35º tilt between Ral's orientation with respect to Raf.[38] Interestingly this tilt has been described as maintaining roughly the same number of hydrogen bonding, hydrophilic and hydrophobic interactions between the two complexes over similar surface areas (1333 $Å^2$ for Ras-Raf and 1331 $Å^2$ for Ras-Ral). [24] The presence of the tilt changes the interactions between so-called switch I region of Ras (identified as residues I28 to R41 in the PDB structure 1LFD) and the RBD of the downstream effector [27]. From the crystal structure and protein modeling, switch I residues D33, P34, I36, E37, D38, S39 and Y40 form hydrophilic interactions with both Raf and Ral.[16] The differences in interactions arise because Ras R41 forms favorable interactions with Raf, but not Ral. Conversely, Ras residues P34 and Y40 show interactions with Ral that are not predicted to be present with Raf. These observations have been the focus of significant discussion to understand how Ras is able to bind to structurally similar but functionally distinct downstream effectors, but are very difficult to confirm because of the lack of a Ras-Raf complex crystal structure. This analysis results in the conclusion that the tilted homologs have a similar number of hydrophobic interactions and hydrogen bonds between the GTPase regardless of which effector is bound,[16] but that these similarities could be replicated by numerous possible orientations of the two proteins. Therefore it would be interesting if this tilt angle could be caused by conserved *electrostatic* interactions, not necessarily conserved *structural* interactions. This would provide additional quantitative information for distinguishing similar complexes and predicting previously unobserved interactions.

4.2 Results

Ras is a protein that is capable of exhibiting remarkable binding discrimination between its various downstream effectors *in vitro* (for example $K_d \sim 20$ nM and $K_d \sim 1$ μM for Raf and Ral respectively). A cursory look through the PDB provides a series of high resolution crystal structures of the homologous GTPase:effector complexes as well as effector monomer structures. These crystal structures demonstrate extensive structural similarities for the homologous GTPases, Ras and Rap, (RMSD < 2 Å for backbone atoms) as well as the downstream effectors, Raf and Ral (RMSD of 3.6 Å for backbone atoms).[16,26,28] Despite these similarities, the docked interaction between the GTPase and Raf *versus* Ral is substantially different, with a 35˚ difference in the orientation of the two effectors in the final docked complex (often referred to as the "tilt" angle in discussions of GTPase-effector structures).[16,38] Although this tilt does change the identity of specific residues interacting between Ras and the effector, the number of possible main chain interactions between the two effectors remains the same.[16,27] Because of this, it has been difficult to justify the reason for the tilt angle or to predict the binding geometry of other, similarly structured downstream effectors without additional crystallography data. The ability to describe the GTPase-effector behavior through optimized electrostatic interactions would therefore be an important tool for investigating protein-protein docking in the absence of crystollographic or NMR structures. To aid in this endeavor, a nitrile probe was placed along eight location of the Raf surface that would be buried in the protein-protein interface upon docking and one additional site that on the surface far removed from the interfacial region. Using the data from simulation, and VSE a

comparison was constructed with a similar study on Ral to highlight regions of similar Stark effect trends.

4.2.1 *Guanosine Dissociation Inhibition Assay.*

Although the small diatomic nitrile probe has been used previously to investigate other protein systems[5,30,54] and DNA[55] it is necessary to determine first whether the probe significantly interferes with the formation of the protein-protein complex that is of interest in the study. The idea that protein structure determines function suggest that if dissociation constant of the interaction between Ras and the nitrile-labeled Rafβ mutant to differ significantly from the purely WT interaction (22 ± 2 nM) then the chemical addition of the nitrile is detrimental to studying the interface. Therefore, the K_d of the docked complex was measured for every construct studied. These results, shown in Table 1, clearly show that K_d of the WT Ras-nitrile labeled Ralβ construct remained essentially unchanged when compared to the purely WT interaction no matter what the location of the nitrile. The only exceptions to this observation were for the mutants $Q66C_{SCN}$ and $K84C_{SCN}$, which both had an increased K_d by a factor of ~2 but still remain roughly an order of magnitude lower than the Ral K_d's reported by Stafford, *et al*.[22]

4.2.2 *Molecular Dynamics Simulations.*

Equation 1-1 tells us that any observed experimental change of the absorption energy of the nitrile probe is due to a change in the local electrostatic environment projected onto the vibrational oscillator's bond axis. This means that the proper interpretation of the VSE experiments relies on knowledge about any changes in orientation from the nitrile probe between docked and monomer experiments.

Additionally the spectroscopic experiment represents an ensemble of probe orientations, and this information cannot be determined from crystal structure alone. Therefore umbrella MD sampling is a useful tool to generate a Boltzmann-weighted ensemble of structures for each nitrile-labeled Rafβ mutant studied. Probability distributions for the χ_2 dihedral on the nitrile in both monomeric (red) and docked complexes (blue) at positions 59, 64, 65, 66, 68, 69, 77, 84, and 90 on Rafβ are shown in Figure 4-1. These probability distributions were generated by biasing the χ_2 dihedral of the cyanocysteine side chain probe in 60º increments for 3 ns each, and calculating the probability of finding a particular angle using WHAM. Simulation convergence was tested by comparing the χ_2 torsional profile of the first 6 ns of simulation with the final 12 ns. A coefficient of determination (R^2) was obtained by subtracting the sum of the squares of the difference in probability for each bin from one. For all simulations, $R^2 > 0.94$, indicating that there was very little difference observed between the first third and last two thirds of any simulation, and our umbrella sampling strategy quickly converged on a statistical ensemble.

The majority of high probability torsional angles follow an alkane distribution with maxima at ±180º and ±60º, as expected for the alkane cyanocysteine. While most nitrile positions freely sampled all available alkane-like rotomers, Figure 4-1 shows that several positions, the $R59C_{SCN}$ and $Q66C_{SCN}$ monomers and the $V69C_{SCN}$ docked complex, were effectively restricted to a single area of alkane-like conformational space. In these cases, examination of individual snapshots was helpful in determining how the chemical details of an individual location would create such striking features in the

ensemble. In the case of $R59C_{SCN}$ and $Q66C_{SCN}$, the monomer torsional motions were restricted because of numerous bulky side chains surrounding those positions. Upon docking these side chains appear to be perturbed by residues comprising the switch I loop of Ras, and in turn grant $R59C_{SCN}$ and $Q66C_{SCN}$ more freedom to sample torsional space. Interestingly, the extreme restricted probability distribution for $Q66C_{SCN}$ may be a large contributing factor to the small standard deviation of monomeric VSE measurements discussed below. Finally, $V69C_{SCN}$ was the only probe location that pointed away from the surface of Rafβ in the monomer but into the interior of Rafβ in the docked complex. This result appeared to arise from a steric interaction with the I41 residue on the binding surface of Ras in the docked complex.

The probability distributions of the χ_2 angles were further used to generate Boltzmann-weighted averages of probe characteristics that depend on an individual probe's torsional distribution, such as the orientation of the probe with respect to WT Ras and the nitrile's solvent accessible surface area (SASA). For each construct, an interfacial binding plane to describe the interactions between the GTPase and the effector were calculated. This in turn allowed us to calculate Boltzmann-weighted averages of the angle of elevation (φ) above and below the interfacial plane and the angle of rotation (θ) about an axis orthogonal to the plane to compare the effect of protein-protein docking on the location and orientation of the nitrile for all nitrile-labeled Rafβ mutants. These data are shown in Figures 4-2 and 4-3. For the angles of rotation (θ) shown in Figure 4-3, the origin of the axes in each panel represents the position of the Cα of the cyanocysteine side chain superimposed on the Ras binding plane. In both figures, the nitrile at position

S77C_{SCN} essentially acts as a control since its distance from the protein-protein interface suggests that its position should not be effected by the formation of the docked complex. Its angle of elevation (φ, Figure 4-2) remains essentially unchanged upon protein docking, while its angle of rotation (θ, Figure 4-3) shows a small change that is well within the standard deviation of the ensemble (shown as a shaded arc around the average). Compared to this control position, there was very little rearrangement upon docking of any probe location with the exceptions of a change in φ for V69C_{SCN} and large changes in θ for mutants Q66C_{SCN} and K84C_{SCN}. Examination of individual snapshots revealed that these large changes in θ seem to arise from a complex series of rearrangements of nearby side chains. For Q66C_{SCN}, for example, the neighboring K65 and R67 residues are pointing away from Rafβ into the solvent during monomeric simulation. These nearby bulky residues push Q66C_{SCN} towards the protein interior where steric hindrances restrict torsional sampling. Upon docking with Ras these bulky neighbor residues are pushed aside to make room for the Ras interface, which coincidently frees the cyanocysteine side chain to move away from the interior of the downstream effector. In much the same manner, K84C_{SCN} is restricted in sample space due to the bulky K87 residue approximately 5 Å away on the monomer. Upon docking with WT Ras, this residue moves away from K84, and the nitrile is allowed to move away from the interior of Rafβ towards the protein-protein interface. These results also explain the larger than usual (~2x) deviations from K_d that both of these mutants experience compared to all other examined constructs.

The MD-generated ensemble of structures was further used to estimate the exposure of each nitrile to solvent water molecules by calculating the SASA for the SCN atoms of each cyanocysteine side chain in the monomeric and docked complexes. These data are shown in Table 2. The SASA values for all probe locations were relatively small compared to the SASA of a fully solvent exposed SCN functional group in a small model compound such as methyl thiocyanate (~130 $Å^2$). The small values of SASA for the nitrile on the monomeric proteins shows that that even while at the protein-solvent interface, these nitrile probes are not significantly exposed to water. This result is consistent with the elevation angles shown in Figure 4-2, which clearly shows that many of the nitrile probes are oriented parallel to the protein surface and therefore only exposed to water on one side of the cyanocysteine side chain. Finally, the data in Table 2 demonstrate that SASA changes between the monomeric and docked complexes were always to lower values upon docking (except for the control position $S77C_{SCN}$, which remained unchanged). Since these residues were selected for nitrile labeling because they become immersed in the docked protein-protein interface upon interface formation and are thus further secluded from water in the docked complex, this observation is expected.

Taken as a whole, the structural data obtained from MD simulations indicate that there is little deviation in probe orientation upon formation of the docked protein-protein interface. With only a few exceptions, which are clearly identified through the simulations, the negligible displacement of the nitrile probe upon forming the docked complex means that observed changes in the vibrational absorption energy of each probe,

discussed below, are the result of changes in electrostatic fields upon moving from the monomeric to docked complexes, and not from extreme probe reorientation.

4.2.3 *Vibrational Stark Effect Spectroscopy.*

Representative spectra of the normalized absorbance for Rafβ K65C_{SCN} both as a monomer (black) and docked with WT Ras (blue) are shown as an example of the data obtained during the VSE experiments in Figure 4-4. Docking with WT Ras increases the absorption energy of the probe by 1.5 ± 0.2 cm^{-1}. Vibrational absorption energy measurements for all positions of the nitrile probe in both the monomeric and docked complexes are shown in Figure 4-5 and enumerated in Table 3. Upon docking, the observed change in absorption energy, $\Delta\bar{\nu}_{obs}$, ranged from a -1.6 cm^{-1} to +1.5 cm^{-1}; of the nine probe locations three experienced a significant shift to lower energies upon docking, while five experienced a significant shift to higher energies. Finally, the absorption energy of our control probe location, S77C_{SCN}, remained constant within experimental error. There is a marked decrease in the full width at half maximum (Δfwhm) of the absorbance when going from monomer to a docked complex for every position with the exception of S77C_{SCN}, complimenting the decrease in SASA values upon formation of the docked complex already discussed.

4.3 Discussion

As shown in Figure 1-8, when Ras binds to the nominally identical downstream effectors Raf and Ral, it induces a tilt angle in the effector that has been of interest to the community since it was first identified in crystal structures.[16,38] This tilt angle has typically been attributed to the need to form favorable salt bridges and hydrogen bonds

between Ras and whatever it is docked with. Analysis of these GTPase-effector complexes has identified a conserved number of main chain interactions between the GTPase and effector as a possible cause of this tilt.[16,26-27,38] Therefore it becomes important to determine whether the tilt angle might actually represent conservation of electrostatic fields at the protein-protein interface, which would highlight a previously unexplained mechanism for determining the orientation of two proteins in a docked complex. The data presented here on changes in absorption energy of nine nitrile probes on Rafβ when docked with WT Ras complement a previous study from our laboratory in which nine nitrile probes on Ralβ were studied after docking with WT Ras both by MD simulations and vibrational absorption energy measurements. These studies were designed to allow a comprehensive comparison between the binding of the two downstream effectors to WT Ras to test the effect of electrostatic fields on the Ras-effector complexes that would not be apparent from examination of crystal structures alone.

Because of the tilt angle, to compare the Ras-Rafβ and Ras-Ralβ interfaces directly it is necessary to determine quantitatively the absolute position of each residue along the surface of Ras, not just the surface of the downstream effector (which is different for the two proteins). This was done by defining a plane along the surface of Ras and dividing that plane into a grid of 75 x 75 bins, each 0.36 $Å^2$ in size. Each bin represents an absolute location on the Ras binding surface; assigning each nitrile probe on Rafβ and Ralβ into one of these bins therefore places that nitrile in an absolute position in the interfacial space along the Ras surface from which it can be compared

directly to the results from the other downstream effector. This surface is shown in Figure 4-6, which is a view of the binding plane from the perspective of the effector showing Ras in ribbon form and highlighting the location of the active site containing GTP and Mg^{2+}. The Boltzmann-weighted location of the midpoint of each nitrile on either Rafβ or Ralβ is shown with a circle determined from the MD simulations for each mutant. These probes were distributed throughout the Ras interfacial binding plane for both downstream effectors, demonstrating that our selection of cyanocysteine mutation locations on Rafβ and Ralβ effectively sampled a large area of the interfacial binding plane. The symbol within the circle indicates the elevation angle, φ, of each probe: $\varphi < \pm 15^{\circ}$ are indicated with a straight line; $\varphi > +15^{\circ}$ (i.e. pointed towards Ras) are indicated with a **X**; and $\varphi > -15^{\circ}$ (i.e. pointed towards the downstream effector) are indicated with a dot (•). Finally, the magnitudes of $\Delta\bar{\nu}_{obs}$ upon binding are colored blue and red for higher and lower energies, respectively, in the docked complex. This figure therefore represents a comprehensive comparison of the energy and position of 18 nitrile probes on two different proteins docked with the same GTPase that is independent of the sequence position or tilt angle of the downstream effector.

The most striking feature of Figure 4-6 is an apparent conservation of Stark shifts along the topology of the Ras interface. There is an area of higher energy shifts centered near the GTP binding site composed of Ralβ residue K32 and Rafβ residues T68 and K84. This conserved region is surrounded by a ring of 9 residues (Rafβ R59, Q66, and V69 and Ralβ I18, R20, N27, N29, Y31, and S33) that are all shifted to lower absorption energy upon biding to Ras. Of the remaining six residues, three (Rafβ G90 and Ralβ N27

and G28) are also clustered within 4 Å of one another on the effector surface; two (Rafβ N64 and K65) do not cluster with any other residues, and one (Rafβ S77) was our control residue located 2 nm away from the interfacial surface plane and therefore not participating in the surface interaction.

These patterns highlight three trends that are easily visualized in Figure 4-6. First, there is a pronounced shift to higher energy upon binding for nitrile probe located inside the switch I loop: Rafβ T68C_{SCN} and K84C_{SCN} and Ralβ K32C_{SCN}. These were the only residues in our study that directly interact with the interior of the switch I region, and all three display similar behavior both in nitrile orientation and absorption energy upon binding. It is likely that the charged Mg^{2+} and the GDPNP molecule are both significant contributing factors to the electrostatic fields experienced by nitrile at these positions along the protein-protein interface because of their high charge/volume ratio and their proximity to the interfacial region. A second significant trend can be seen with the residues interacting with the switch II of Ras shown on the right-hand side of figure 4-6. Of the nine residues tested, three came from Rafβ (R59, Q66 and V69), and six came from Ralβ (I18, R20, N29, S33, Y31, and N54). With the exception of Rafβ V69C_{SCN}, all residues in this region shifted to lower energy shift upon docking. Rafβ V69C_{SCN} is is the sole residue in the region with an angle of elevation below the binding plane < -15º and is the only one within the region with an absorption shift to higher energy. This observation highlights the need to fully understand nitrile geometry to interpret VSE data. The third trend is revealed by comparing Rafβ G90C_{SCN} with Ralβ N27C_{SCN} and G28C_{SCN}. All three residues experience a blue shift upon docking with WT Ras.

Interestingly, when overlaying the crystal structures of the Rap-Raf complex with the Ras-Ral complex, the Cα carbons for Rafβ $G90C_{SCN}$ and Ralβ $G28C_{SCN}$ sit less than 1 Å away from one another. However, the nitrile distribution from simulation indicates the locations of the VSE probes between the two effectors are situated more than twice that amount, ~2.3 Å, away from one another in the Ras plane.

The conserved patterns observed for Ras docking with two downstream effectors, Rafβ and Ralβ, demonstrate an electrostatic origin for the binding interaction between a single protein and two structurally similar but sequence disparate downstream effectors; maintaining these electrostatic interactions causes differences in binding orientation of the two downstream effectors. Previous rationalization of these differences in binding orientation have focused on factors that can be inferred from the crystal structures, such as hydrogen bonding and salt bridge formation.[26-27] The conservation of electrostatic fields at the Ras-effector interface shown clearly in Figure 4-6 provides an alternative and generalizable rational; binding orientation of the downstream effector is determined by a pattern of complimentary electrostatic fields that are maximized in the final, docked configuration. An additional crystal structure of Ras bound to the downstream effectors PI3Kγ has also been determined [24]. This similarly shaped downstream effector docks with the binding plane of Ras to form an overall surface area of ~1300 $Å^2$, very similar for Ras-Raf and Ras-Ral discussed above.[24] Further experiments in our laboratory will determine whether electrostatic interactions as described by VSE experiments are conserved in this docked interaction as well. The discovery of such a robust pattern of electrostatic fields between three structurally similar but functionally distinct downstream

effectors with the switch I loop of Ras will provide robust modeling and predictive capabilities for studying this physiologically critical protein-protein interface.

In conclusion, the 35˚ tilt in the binding angle of Ral when compared to Raf has been a subject of significant past discussion, but its physical origins have not been well described.[16,27,38] The work presented here shows quantitatively that this tilt angle is not only preserving a quantity of structural interactions including hydrogen bonds and hydrophobic interactions, as described previously in examination of crystal structures,[16,24,26-27,38] but also by a pattern of noncovalent electrostatic interactions between the two downstream effectors. This conservation of electrostatic and structural interactions is a driving force that causes two structurally identical proteins to assume a different orientation in the lowest-energy interaction with Ras. With the emergence of this new VSE data set, there is now a new level of complexity to explore and model previously described interactions. More generally, adding the role of electrostatics to other, more traditional measures of protein interactions such as hydrogen bonds or salt bridges expands the complexity and accuracy with which protein-protein interactions can be described and understood both in experimental studies and in molecular modeling.

Table 4-1:. Dissociation constant (K_d) of WT Ras docked with WT Raf and nine Rafβ mutants obtained by fitting k_{obs} from the GDI assay to Equation 2. Errors are reported as one standard deviation of at least 3 experimental replicates.

Rafβ Mutant	K_d (nM)
WT	22 ± 2
$R59C_{SCN}$	32 ± 4
$N64C_{SCN}$	29 ± 5
$K65C_{SCN}$	37 ±7
$Q66C_{SCN}$	44 ±8
$T68C_{SCN}$	27 ± 2
$V69C_{SCN}$	25±3
$S77C_{SCN}$	24 ± 4
$K84C_{SCN}$	42± 6
$G90C_{SCN}$	30 ± 10

Table 4-2: Solvent accessible surface area (SASA) calculated for each of the nine Rafβ mutants. Both monomer and docked are shown. Errors are reported as one standard deviation of a Boltzmann-weighted ensemble of structures.

Rafβ Mutants	Monomer SASA ($Å^2$)	Docked SASA ($Å^2$)
$R59C_{SCN}$	40 ± 10	40 ± 10
$N64C_{SCN}$	50 ± 10	40 ± 20
$K65C_{SCN}$	56 ± 6	40 ± 10
$Q66C_{SCN}$	23 ± 8	12 ± 4
$T68C_{SCN}$	20 ± 10	13 ± 4
$V69C_{SCN}$	40 ± 10	20 ± 10
$S77C_{SCN}$	22 ± 8	22 ± 8
$K84C_{SCN}$	52 ± 8	50 ± 10
$G90C_{SCN}$	30 ± 1	20 ± 10

Table 4-3: Vibrational Stark Effect measurements of the nine Rafβ mutants. Changes in absorption energy ($\Delta\nu_{obs}$) and full width at half maximum (Δfwhm) are reported as the monomer values subtracted from the docked complex values.

	Monomer		Docked with WT Ras		
Rafβ Mutants	ν (cm^{-1})	*fwhm*(cm^{-1})	$\Delta\nu_{obs}$ (cm^{-1})	Δ*fwhm*(cm^{-1})	$\Delta\vec{F}_{prote}$(MV/cm)
$R59C_{SCN}$	2161.5 ± 0.4	12.9 ± 0.2	-1.6 ± 0.4	-2.3 ± 0.5	2.1
$N64C_{SCN}$	2160 ± 0.3	10.6 ± 0.4	-0.6 ± 0.2	-1.2 ± 0.1	0.8
$K65C_{SCN}$	2161.1 ± 0.1	10.7 ± 0.9	1.5 ± 0.2	-1.4 ± 0.0	-1.9
$Q66C_{SCN}$	2160.8 ± 0.02	14.4 ± 0.9	-0.4 ± 0.3	-5.6 ± 0.3	0.5
$T68C_{SCN}$	2162.3 ± 0.3	13.1 ± 0.5	0.2 ± 0.1	-6.4 ± 0.0	-0.3
$V69C_{SCN}$	2162.1 ± 0.2	13.8 ± 0.5	0.3 ± 0.1	-0.7 ± 0.6	-0.4
$S77C_{SCN}$	2160.2 ± 0.3	11.6 ± 0.1	-0.1 ± 0.3	-0.3 ± 0.5	0.1
$K84C_{SCN}$	2158.7 ± 0.5	12.6 ± 0.3	1.3 ± 0.4	-1.3 ± 0.5	-1.7
$G90C_{SCN}$	2159 ± 0.2	9.0 ± 0.6	0.4 ± 0.2	-1.2 ± 0.9	-0.5

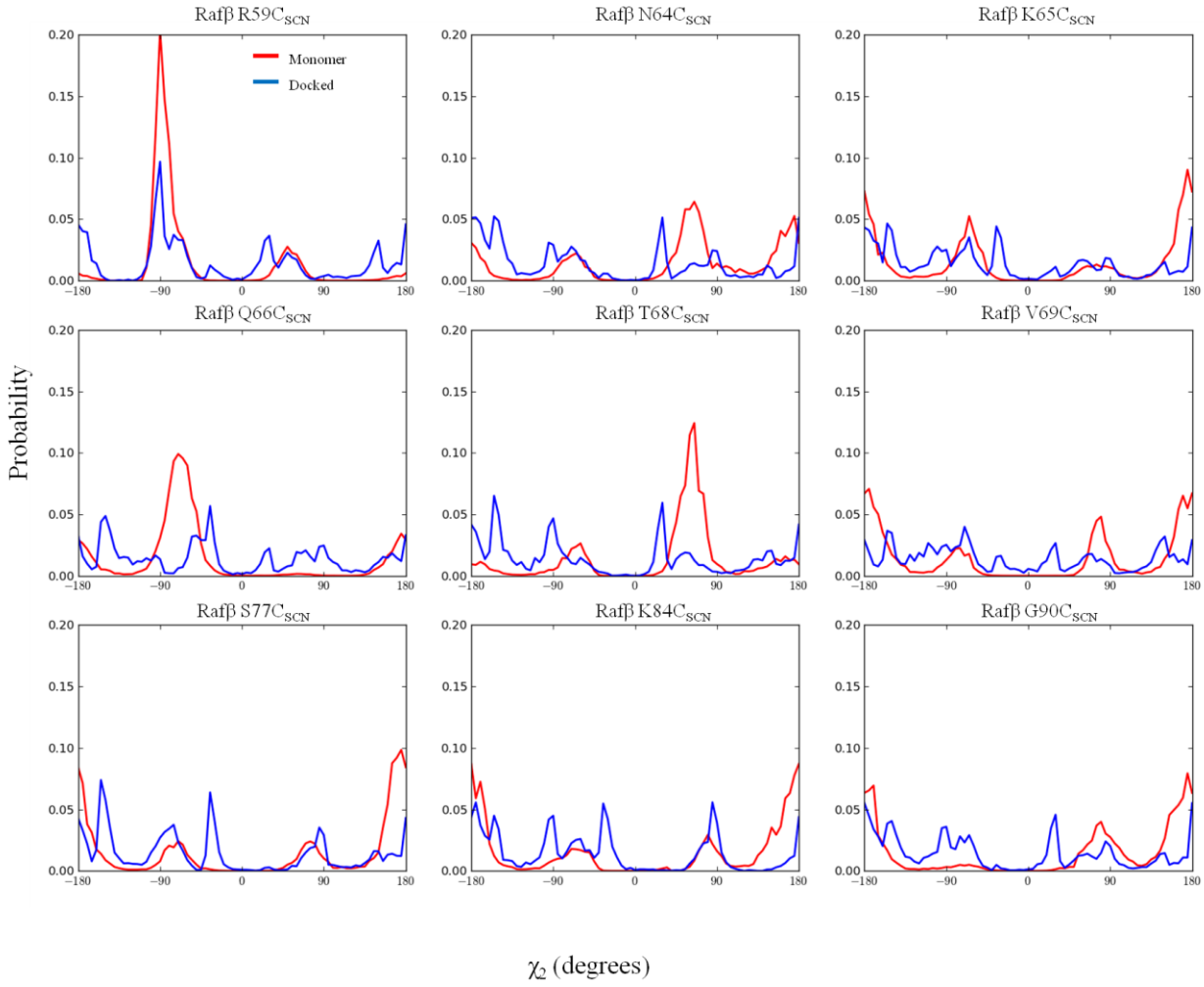

Figure 4-1 Boltzmann-weighted χ2 probability distribution for each of the nine Rafβ probes

Monomer distributions are shown in red, and docked distributions are shown in blue. For most residues the predicted "alkane" like distribution is observed with the exception of the Q66C$_{SCN}$ monomer distribution.

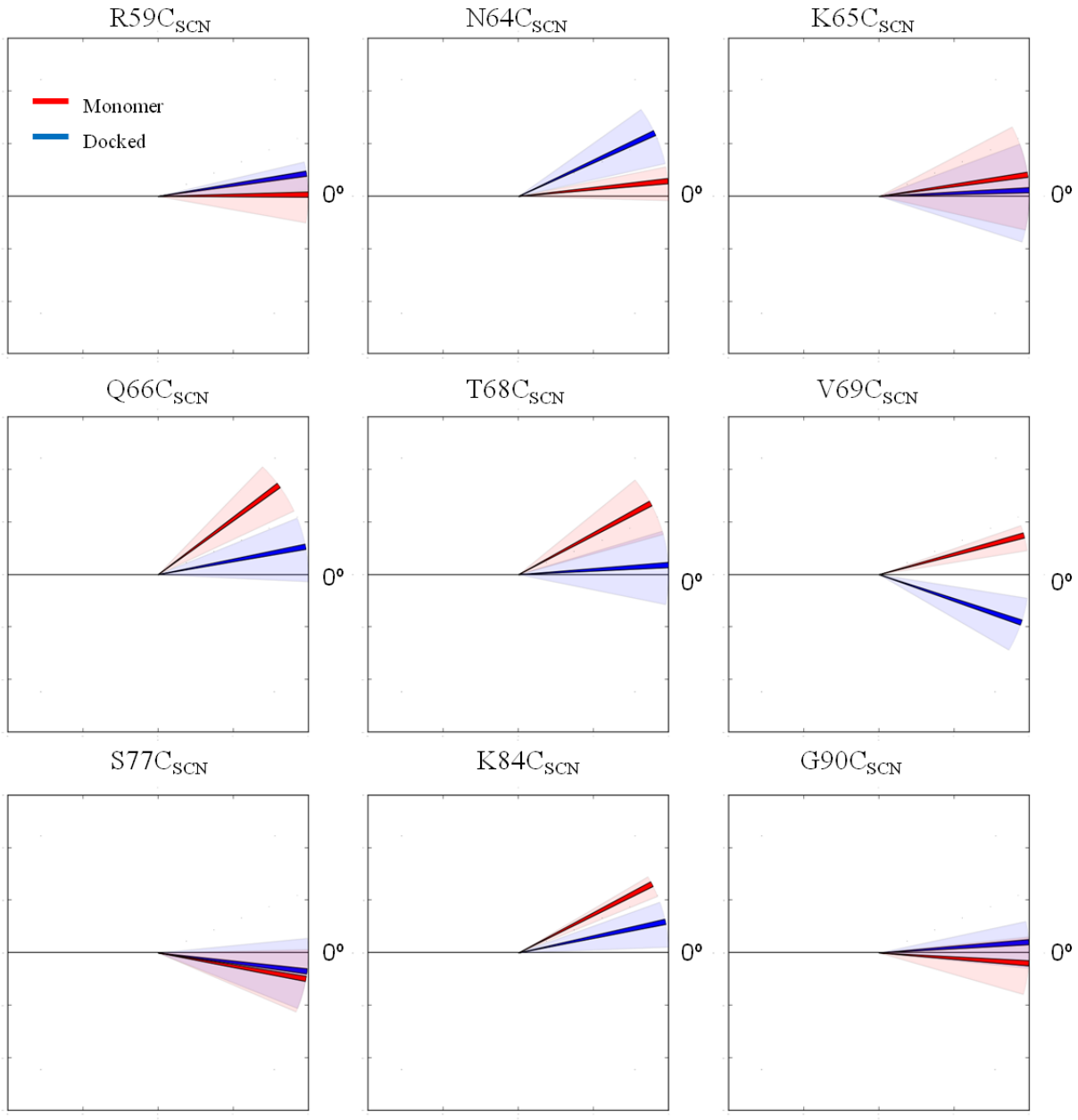

Figure 4-2 Boltzmann-weighted azimuthal angles of the nine probe locations on Rafβ

The solid lines represent the averages of the azimuthal angle, while the shaded areas represent one standard deviation from MD simulations. Monomer results are shown in red, docked results are shown in blue.

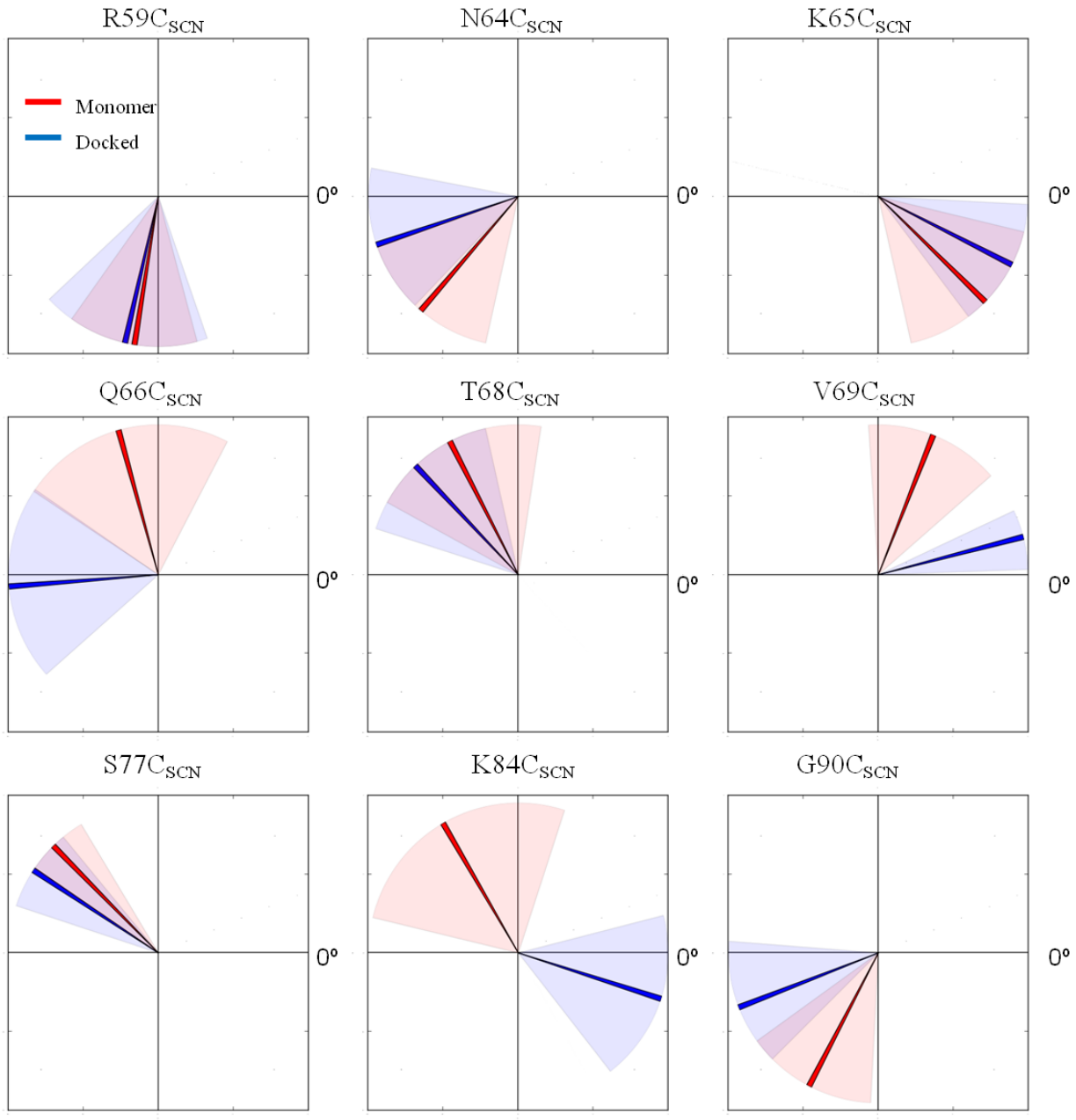

Figure 4-3 Boltzmann-weighted polar angles of the nine probe locations on Rafβ

The polar angles are in respect to an axis centered on the origin of each panel that is orthogonal to a binding plane between Raf and Ras. The solid lines represent the averages of the angle, while the shaded areas represent one standard deviation from MD simulations. Monomer results are shown in red, docked results are shown in blue.

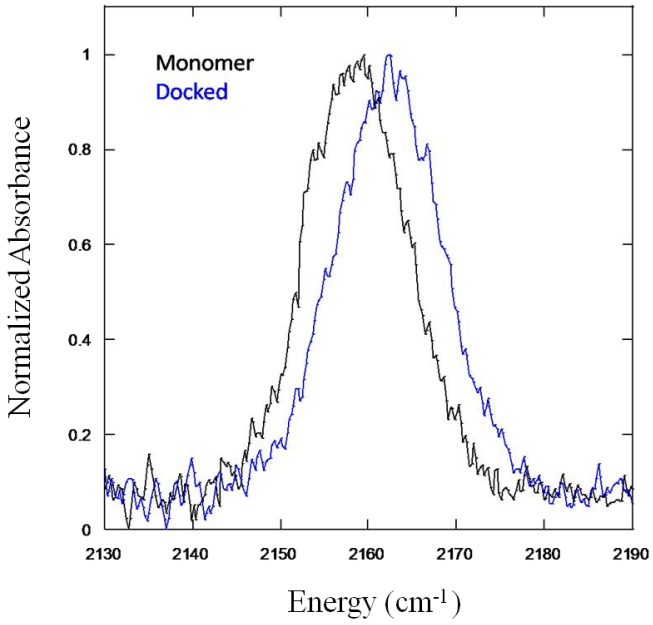

Figure 4-4 Representative Stark effect spectra for Rafβ

Representative spectra of Rafβ K65C$_{SCN}$ of both the monomer (black) and docked with WT Ras (blue), separated by a shift of 1.5 cm^{-1}.

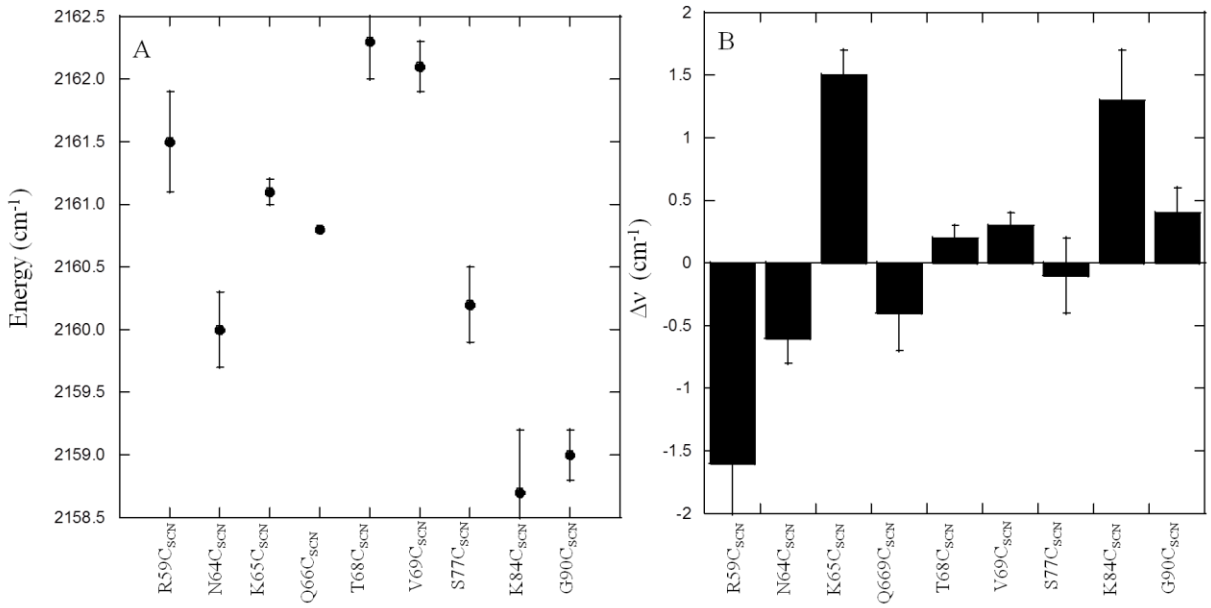

Figure 4-5 Comparison of the nine Rafβ probes docked vs monomer absorption energies

A: Absolute absorption energy of each SCN-labeled Rafβ monomer. B: $\Delta\nu_{obs}$ of each SCN-labeled Rafβ docking with WT Ras with respect to the monomeric absorption energy. Standard deviations are the results of at least three replicates.

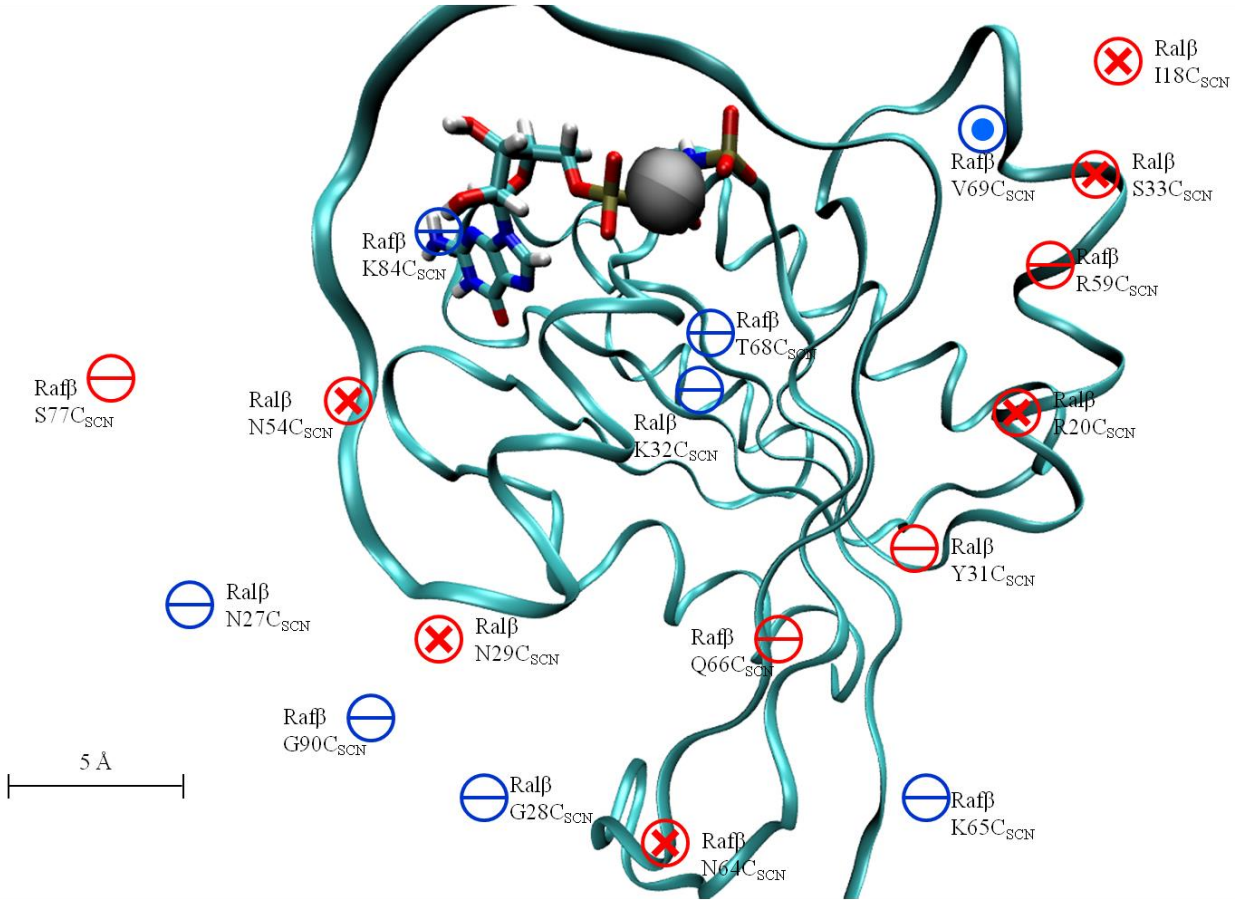

Figure 4-6 Comparison of the VSE and MD results between the Ras – Raf and Ras – Ral complexes.

The cyan ribbon diagram represents the effector binding region of Ras. Circles represent Boltzmann-weighted averages of the location of the nitrile midpoint projected on a plane built by least squares fitting of the Ras switch I Cα carbons. Blue circles represent $\Delta\nu_{obs} > 0$, and red circles represent $\Delta\nu_{obs} < 0$, upon binding with WT Ras. The symbol within each circle represent the angle of elevation of the nitrile with respect to the Ras binding plane. Lines: nitrile probe is parallel (±15º) with respect to the Ras effector binding plane; **X:** nitrile probe is pointed into Ras (>15˚); •: nitrile probe pointed away from Ras (>-15˚) and thus into the effector. Ralβ spectroscopic information was taken from Stafford, *et al.*[22]

Chapter 5 Vibrational Stark Effect Spectroscopy and Molecular Dynamics Simulation Reveal Long Range Electrostatic Changes Due Mutations to Glutamine 61 on Ras

5.1 Introduction

Ras represents an interesting target for oncology research because mutations to Ras are found in nearly 30% of human cancer tumors.[56] Most notably, many of these mutations inhibit the ability of Ras to perform GTP hydrolysis leaving it in a constitutively ON state where uncontrolled cellular signaling occurs. Most oncogenic forms of Ras involve mutations at positions G12, G13 and Q61.[9,57-60] Glycines 12 and 13 are situated within the ligand binding site of Ras, and any mutations will sterically preclude normal function of GTPase activity. Glutamine 61 is of particular interest because of the role it is believed to play in the hydrolysis of GTP to GDP, a necessary step in switching Ras to the inactive OFF state. Intrinsic GTP hydrolysis by Ras is a slow process occurring at a rate of ~ 1.2 x 10^{-4} s^{-1} that is sped up considerably to a rate of 14 s^{-1} by interactions with a GTPase Activating Protein (GAP).[61-62] This 10^5 rate increase is accomplished by introducing an arginine finger domain into the active site of Ras that can help orient water molecules for stabilizing transition intermediates. The role of Q61 in this process is not fully understood, but studies of mutations at Q61 using crystallography,[63-64] kinetics,[65] and theoretical modeling[65-66] have indicated that the glutamine does not participate chemically in the hydrolysis reaction, but instead is

Chapter 3 is based on work previously published.
Stafford, A. J.; Walker, D. M.; Webb, L. J. *Biochemistry* **2012**, *51*, 2757.
Lauren Webb supervised the work. Amy Stafford was a graduate student who performed VSE spectroscopy and GDI assay on the mutants.

responsible for stabilizing the structural and electrostatic organization of the active site, which in turn allows the so-called "arginine finger" or RasGAP to stabilize a highly polar transition state caused by nucleophilic attack on the γ-phosphate of GTP.[64,66] This proposed mechanism is shown below in Figure 5-1.

In an effort to investigate the role position 61 plays in GTP hydrolysis, Q61 was mutated to 18 different amino acids to represent all possible variations at position 61 with the exception of cysteine or proline which could not be expressed. Each of these constructs were then probed using the nitrile-labeled Ralβ I18C_{SCN} in multiple VSE experiments. The vibrational absorption energy of each mutant was then compared to the wild type absorption energy. Through MD sampling, a Boltzmann weighted ensemble of position 61 torsions was obtained and used to calculate solvent accessible surface area (SASA) for the residue at position 61. It was found that there was a high degree of correlation between the simulated SASA calculations and the vibrational energy for the mutants. This correlation was also seen between the absorption energy of each mutant and the hydration potential of each residue at pH 7. These correlations support the hypothesis of Q61 being responsible for stabilizing water molecules in the active site during GTP hydrolysis.

5.2 Results

5.2.1 *Guanosine Dissociation Inhibition Assay*

Any mutation to a protein needs to be carefully considered and tested to ensure that it does not abolish function. To screen for the potential of a deleterious mutation each construct of Ras was subjected to the GDI assay established by Herrmann *et al* by Ms.

Amy Stafford.[26,48] The results of kinetics assay are tabulated below in table 5-1. Although there is a marked increase in K_d for some mutations, it has been established by Stafford *et al*. that the kinetic data demonstrate that there is no significant disruption of binding between Ralβ $I18C_{SCN}$ and the position 61 mutants of Ras.[48]

5.2.2 *VSE Spectroscopy of Ras Q61X-Ralβ $I18C_{SCN}$ Complexes*

Vibrational Stark effect spectroscopy was performed by Ms. Stafford, and is presented below in table 5-2. The absorption energies of the thiocyanate on Ralβ $I18C_{SCN}$ docked with each Ras Q61X mutant are compiled in Table 2, and demonstrate that certain amino acid substitutions at position 61 do indeed cause a change in absorption energy of the thiocyanate probe. This observation was used to test the hypothesis that various side chain characteristics of each mutant influence the electrostatic fields in the vicinity of the nitrile probe.

To test the hypothesis that position 61 actively stabilizes a water molecule during intrinsic GTP hydrolysis by Ras were true, it would be necessary to find a way to measure each side chains interactions with solvent. The two measurements of the affinity of the amino acid side chain for water that best describe these water interactions would be the SASA of the polar components of the side chain and the hydration potential of each residue. The calculated SASA for the entire residue (including backbone atoms), the entire side chain, and only the polar components of the amino acid are shown in Table 5-3. These values of SASA were determined by assembling a Boltzmann-weighted ensemble of structures of each Ras Q61X mutant docked with Ralβ $I18C_{SCN}$, and thus represent a sample that specifically took into account any steric occlusion of water

molecules around position 61 from nearby amino acid residues on either Ras or Ralβ $I18C_{SCN}$. When these calculated values of polar SASA are compared to the values previously reported by Wimley *et al*.(e.g. SASA calculated on peptides AcWL-X-LL and AcGG-X-GG (where X was each amino acid)),[67] there is a demonstrable correlation between SASA and hydration potential with values of $r = 0.84$. These SASA values reported where determined from Boltzmann-weighted ensembles of Ras Q61X-Ralβ $I18C_{SCN}$ structures and therefore most accurately reflect the exact structural realities of this system versus those reported by a model like Wimley's. These data are therefore an appropriate estimate of the extent to which the polar, hydrophilic component of each residue interacts with water in the Ras active site.

In Figure 5-2, the polar SASA of each amino acid side chain are compared to the thiocyanate absorption energies, ν_{obs}, of Ras Q61X mutants docked with Ralβ $I18C_{SCN}$. The correlation between polar SASA and observed vibrational frequency in Figure 5-2was found to be $r = 0.72$ if the seven residues with no polar surface area (Ala, Met, Phe, Gly, Leu, Val, and Ile) were excluded. This high correlation suggests that changes in the electrostatic environment of the probe can be related directly to the total polarity of the residue at position 61 of Ras through the ability of that residue to interact with water. The negative slope of the correlation implies that absorption energy of the probe increases as the side chain's affinity towards water decreases, thus potentially reducing the number of waters in the immediate vicinity of the thiocyanate probe. The effect is not simply steric; a plot of the total side chain SASA versus the observed vibrational absorption energy was essentially random, with $r = 0.1$ (data not shown).

Furthermore, the ability of the side chain to interact with water was measured by the metric of hydration potentials for each residue. In Figure 5-3, a comparison the hydration potentials, tabulated at pH = 7 by Wolfenden, *et al*.,[68] to the measured ν_{obs} for each Ras Q61X mutation is made. As in Figure 5-1, the data is divided into mutants composed of polar versus nonpolar residues. When considering polar residues, there is a strong correlation between hydration potential and absorption energy of $r = 0.72$ (Arg is again an outlier, and if this is excluded from the least squares fit, $r = 0.86$). When only the nonpolar residues are considered, there is a much smaller correlation between the hydration potential and vibrational absorption energy, $r = 0.34$. This discrepancy arises because there is a much smaller range in hydration potential for the hydrophobic residues (< 4 kcal/mol) while there is a much larger range for the polar residues (~ 15 kcal/mol) For both polar and nonpolar residues, the absorption energy increases with increasing hydration potential, i.e. increasingly unfavorable interactions between the side chain and water. The trend presented in figures 5-2 and 5-3 describe that the absorption energy of the thiocyanate probe increases as the ability of the side chain at position 61 to interact favorably with water decreases.

In previous work describing 11 thiocyanate probe locations on the surface of Ralβ, Ms. Stafford, *et al*. measured a significant difference in absorption energy of the vibrational probe based on its position on the surface of the monomeric, undocked protein.[22] Using molecular dynamics sampling, they generated a Boltzmann-weighted ensemble of structures of each SCN-labeled Ralβ mutant, and measured the total SASA of each thiocyanate probe.[22] They found that the absorption energy increased as the

SASA decreased, i.e. as the probe was exposed to less water.[41] This was interpreted as a Stark shift caused by the relative exposure of each probe to the electrostatic field generated at the protein-water interface which differed based on the exposure of a probe at each location to water. By correlating the change in absorption energy of the thiocyanate probe at Ralβ I18C$_{SCN}$ in the present study with two measures of water affinity, polar SASA and hydration potential of the residue, we have now observed that the thiocyanate probe responds in a predictable way to the local electrostatic environment working to stabilize or destabilize the presence of water.

Polarity is a complex chemical phenomenon generated by molecular multipole moments, and influencing numerous measurable parameters such as solvation free energy, hydrogen bonding ability, solvent interactions, and reactivity. Polarity is a particularly important concept at position 61 of Ras because of previous experimental and computational studies that have linked the glutamine at that position to the ability of Ras to stabilize a water molecule near or in its active site, which in turn influences the rate of GTP hydrolysis through both intrinsic and induced mechanisms. The value of examining this phenomenon with a vibrational probe that is sensitive to electrostatic fields, such as the thiocyanate, is that the measured change in vibrational absorption energy can be directly correlated to a change in the electrostatic environment of the probe caused by mutations at Ras Q61 and projected onto the probe bond, $\Delta\vec{F}_{Q61X}$ (presented as $\Delta\vec{F}_{protein}$ in equation 1-1). The measured values of $\Delta\vec{F}_{Q61X}$ are tabulated in Table 5-2, ranked from largest positive to largest negative shift. While two charged residues with nonzero polar

surface areas (Arg and Asp) increased the local electrostatic field of the probe (and Asn lead to a negligible change), all other polar residues caused a decrease in the local electrostatic field of up to -2.7 MV/cm. For the amino acids with no nonpolar surface area, although the trend of decreasing field was also observed, there was a significantly lower correlation of this effect to the hydration potential of these residues (dashed line in Figure 5, $r = 0.34$) and no correlation to size or steric parameters (Figure 4). Any significant structural change of amino acids in the vicinity of the nitrile probe would make comparison of vibrational energy differences between polar and nonpolar residues difficult. Furthermore, interpreting the presence of water molecules in and near the Ras active site is only valid when the protein is in an ordered, catalytic configuration. This occurs when Ras is docked to a downstream effector, our extensive Boltzmann-weighted molecular dynamics sampling could provide some clues to a structural basis for differences between polar and nonpolar residues. These structures are used to investigate three structural parameters: 1) rmsd of the backbone in the loop region containing Q61X (residues 59 – 62) compared to residues in a α-helix far away from this site, 2) the angle of the side chain at position 61 with respect to the Ras-Ral interfacial plane, and 3) the orientation of the side chain with respect to an axis perpendicular to the surface plane containing both Ras Q61X and Ralβ $I18C_{SCN}$.

Residue 61 lies in a loop region of the Ras structure, and therefore could be more prone to structural rearrangement upon mutagenesis. Because our MD simulation strategy resulted in converged structures after 18 ns of simulation time, we tested the rmsd of backbone atoms for the loop region, residues 59 – 62, compared with that of 4

residues residing in a stable α-helix far away from this site, residues 92 – 95. Although the rmsd of the loop region, 0.33 ± 0.03 Å, was slightly larger than the control region, 0.22 ± 0.01 Å, this is still too small to suggest that there is large scale rearrangement of the backbone caused by mutations at Ras Q61. There was, however, a trend towards higher rmsd of nonpolar residues at position 61 compared with the polar residues (0.35 ± 0.03 Å versus 0.32 ± 0.02 Å, respectively) that was not observed at the control position. Although these structural fluctuations are still small, along with the generally higher K_d values for nonpolar residues, it is further indication that nonpolar side chains at position 61 may lead to instability in that part of the protein.

Although the backbone appears to be very stable, it is possible that the orientation of the side chain at position 61 could change dramatically depending on the mutant. To investigate this, two parameters for each side chain are defined which are equivalent to polar (ϕ) and azimuthal (θ) angles in spherical polar coordinates. The mathematical definitions of these two angles have been introduced extensively elsewhere[39] and in great detail in chapter 2.4; those definitions are not detailed here because there was essentially no differences in these two structural parameters for any side chain at Ras position 61 when measured. The sole exception to this was a rotation of the indole group of Ras Q61W in order to relieve steric repulsions between the Trp side chain and the GDPNP nucleotide. No other significant structural motions were observed in the molecular dynamics sampling of torsional motions at this location.

5.3 Discussion

Here VSE spectroscopy was used to probe electrostatic effects on protein-protein interactions in pathological and carcinogenic Ras mutants to learn how mutations in Ras at glutamine 61 influence the function of Ras-effector interfaces to characterize in detail the difference between WT Ras and cancer-causing mutants. Interestingly, changes in the vibrational absorption energy of an appropriately placed thiocyanate probe are shown to be directly correlated to the polar surface area of side chains at position 61 of Ras as determined by simulation. Furthermore, the vibrational absorption energy was correlated to changes in hydration potential of all side chains, although the correlation was much stronger for residues containing polar character than it was for residues only containing nonpolar functionality. This study demonstrates that the ability of position 61's to interact with active site waters causes long range electrostatic changes as revealed by VSE spectroscopy in the Ras binding interface. These long range electrostatic interactions provide an interesting area of research in how mutations of Ras can cause harmful oncogenic behavior and indicate a need for continued research.

Table 5-1. Binding kinetics of Ralβ I18C_{SCN} docked to WT Ras and Ras Q61X mutants. Error is reported as one standard deviation of multiple experiments. Data provided by Ms. Amy Stafford.

Ras Q61X Mutation	K_d (μM)
WT	2.6 ± 0.2
Q61A	18.8 ± 0.7
Q61D	13.0 ± 0.6
Q61E	11.7 ± 0.4
Q61F	36.2 ± 0.8
Q61G	8.8 ± 0.3
Q61H	22.2 ± 0.2
Q61I	7.0 ± 0.6
Q61K	4.1 ± 0.7
Q61L	2.4 ± 0.3
Q61M	7.8 ± 0.3
Q61N	2.6 ± 0.2
Q61R	15.9 ± 0.7
Q61S	20.4 ± 0.9
Q61T	28.1 ± 0.7
Q61V	5.9 ± 0.9
Q61W	39.6 ± 1.0
Q61Y	31.7 ± 0.8

Table 5-2. Measured SCN vibrational frequencies (ν_{obs}) of Ralβ I18C$_{SCN}$ docked with WT Ras and Ras Q61X mutants; the measured difference in absorption ($\Delta\nu_{obs}$) and field ($\Delta\vec{F}_{Q61X}$) of Ras Q61X mutants versus WT Ras; measured full width at half maximum (fwhm) of Ralβ I18C$_{SCN}$ docked with WT Ras and Ras Q61X mutants and the difference (Δfwhm) of Ras Q61X mutant versus WT Ras. Error in ν_{obs} and fwhm is one standard deviation from multiple experiments. Error in $\Delta\nu_{obs}$ is linearly propagated error from the measurement of WT Ras versus Ras Q61X. Fields were calculated using equation 1-2. Data provided by Ms. Amy Stafford.

Ralβ I18C$_{SCN}$ Bound to:	ν_{obs} (cm^{-1})	$\Delta\nu_{obs}$ relative to WT Ras (cm^{-1})	$\Delta\vec{F}_{Q61X}$ (MV/cm)	fwhm (cm^{-1})	Δ fwhm (cm^{-1})
WT Ras	2162.8 ± .2	0.0	0.0	12.8 ± 0.5	0.0
Residues with some hydrophilic character					
Ras Q61D	2162.0 ± .1	-0.8 ± 0.2	1.1	13.9 ± 0.1	1.1
Ras Q61R	2162.4 ± .1	-0.4 ± 0.2	0.6	14.6 ± 0.1	1.8
Ras Q61N	2162.7 ± .2	-0.1 ± 0.3	0.1	13.2 ± 0.2	0.4
Ras Q61E	2162.8 ± .2	0.0 ± 0.3	0.0	12.8 ± 0.7	0.0
Ras Q61K	2163.1 ± .3	0.3 ± 0.3	-0.4	12.8 ± 0.3	0.0
Ras Q61Y	2163.5 ± .1	0.7 ± 0.2	-1.0	13.9 ± 0.2	1.1
Ras Q61H	2163.8 ± .2	1.0 ± 0.3	-1.4	13.6 ± 0.4	0.8
Ras Q61W	2164.1 ± .2	1.3 ± 0.3	-1.9	13.7 ± 0.2	0.9
Ras Q61S	2164.4 ± .1	1.6 ± 0.2	-2.3	13.4 ± 0.3	0.6
Ras Q61T	2164.7 ± .2	1.9 ± 0.3	-2.7	12.4 ± 0.3	-0.4
Residues with no hydrophilic character					
Ras Q61A	2162.0 ± .2	-0.8 ± 0.3	1.1	13.4 ± 0.4	0.6
Ras Q61M	2162.6 ± .1	-0.2 ± 0.2	0.3	13.6 ± 0.1	0.8
Ras Q61F	2163.0 ± .2	0.2 ± 0.3	-0.3	13.6 ± 0.2	0.8
Ras Q61G	2163.1 ± .1	0.3 ± 0.2	-0.4	13.8 ± 0.6	1.0
Ras Q61L	2163.2 ± .2	0.4 ± 0.3	-0.6	12.0 ± 0.6	-0.8
Ras Q61V	2163.9 ± .0	1.1 ± 0.2	-1.6	14.2 ± 0.2	1.4
Ras Q61I	2164.0 ± .2	1.2 ± 0.3	-1.7	13.1 ± 0.1	0.3

Table 5-3. Calculated SASA for 16 of the Ras Q61X mutations from the Boltzmann weighted torsional distributions. "Entire residue" includes all of the atoms in the calculations, "side chain" only includes atoms from the side chain, and "polar atoms" are nitrogens, oxygens, and any hydrogens bonded to them. Error is reported as one standard deviation from the SASA calculation preformed on the 16 structures of the Boltzmann-weighted ensemble.

Ralβ I18C_{SCN} Bound to:	Entire residue ($Å^2$)	Side Chain ($Å^2$)	All Polar Atoms ($Å^2$)	Side Chain Polar Atoms ($Å^2$)
WT Ras	250 ± 10	179 ± 7	230 ± 17	114 ± 4
Residues with some hydrophilic character				
Ras Q61D	216 ± 7	150 ± 6	200 ± 12	110 ± 4
Ras Q61R	290 ± 11	226 ± 8	144 ± 6	144 ± 6
Ras Q61N	222 ± 9	154 ± 6	210 ± 20	114 ± 4
Ras Q61E	242 ± 9	175 ± 6	230 ± 10	109 ± 5
Ras Q61K	260 ± 10	198 ± 8	202 ± 7	82 ± 2
Ras Q61Y	290 ± 10	230 ± 10	198 ± 4	77 ± 1
Ras Q61H	260 ± 10	191 ± 8	220 ± 20	114 ± 5
Ras Q61W	330 ± 20	270 ± 20	198 ± 7	80 ± 1
Ras Q61S	187 ± 6	118 ± 4	166 ± 8	77 ± 1
Ras Q61T	209 ± 7	145 ± 5	162 ± 7	77 ± 1
Residues with no hydrophilic character				
Ras Q61M	261 ± 10	194 ± 5	121 ± 3	0 ± 0
Ras Q61F	280 ± 10	220 ± 10	122 ± 3	0 ± 0
Ras Q61L	244 ± 9	182 ± 5	121 ± 3	0 ± 0
Ras Q61V	220 ± 7	159 ± 5	121 ± 3	0 ± 0
Ras Q61I	242 ± 8	183 ± 6	121 ± 3	0 ± 0

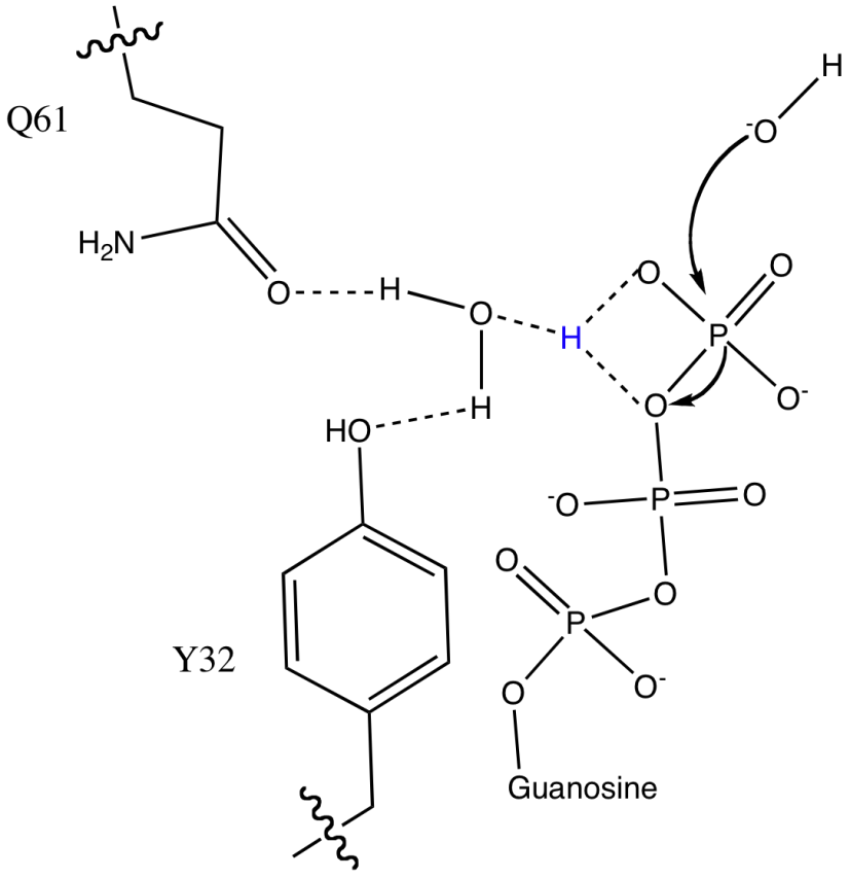

Figure 5-1 Proposed model of Q61 role in Ras GTP hydrolysis

Proposed mechanism for intrinsic GTP hydrolysis by Ras, showing Q61 hydrogen bonding to a developing H_3O^+ formed from a hydrogen atom (blue) transferred from a catalytic water molecule. Adopted from Buhrman *et al*.[64]

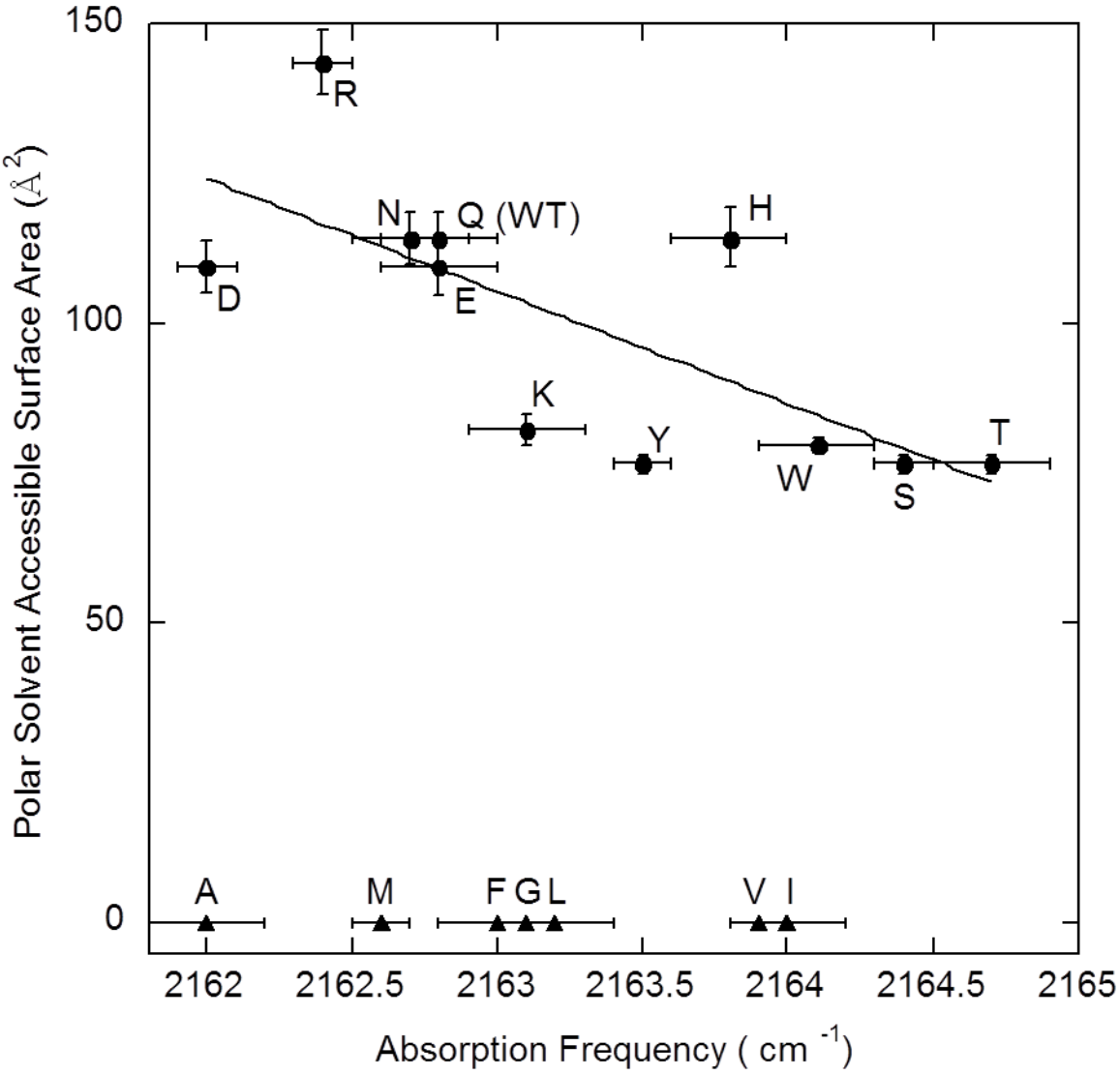

Figure 5-2 Comparison of side chain SASA with absorption energies

Solvent-accessible surface area of polar side chain components compiled from molecular dynamics trajectories of Ras Q61X mutants versus the measured ν_{obs} of Ralβ I18C$_{SCN}$ docked Ras Q61X mutants. Circles: hydrophilic residues; triangles: hydrophobic residues. The correlation for hydrophilic residues is $r = 0.72$. Error bars on ν_{obs} represent one standard deviation from multiple measurements. Error bars on SASA measurements represent one standard deviation of a Boltzmann-weighted ensemble of 18 ns of molecular dynamics trajectories for each Ras Q61X mutant.

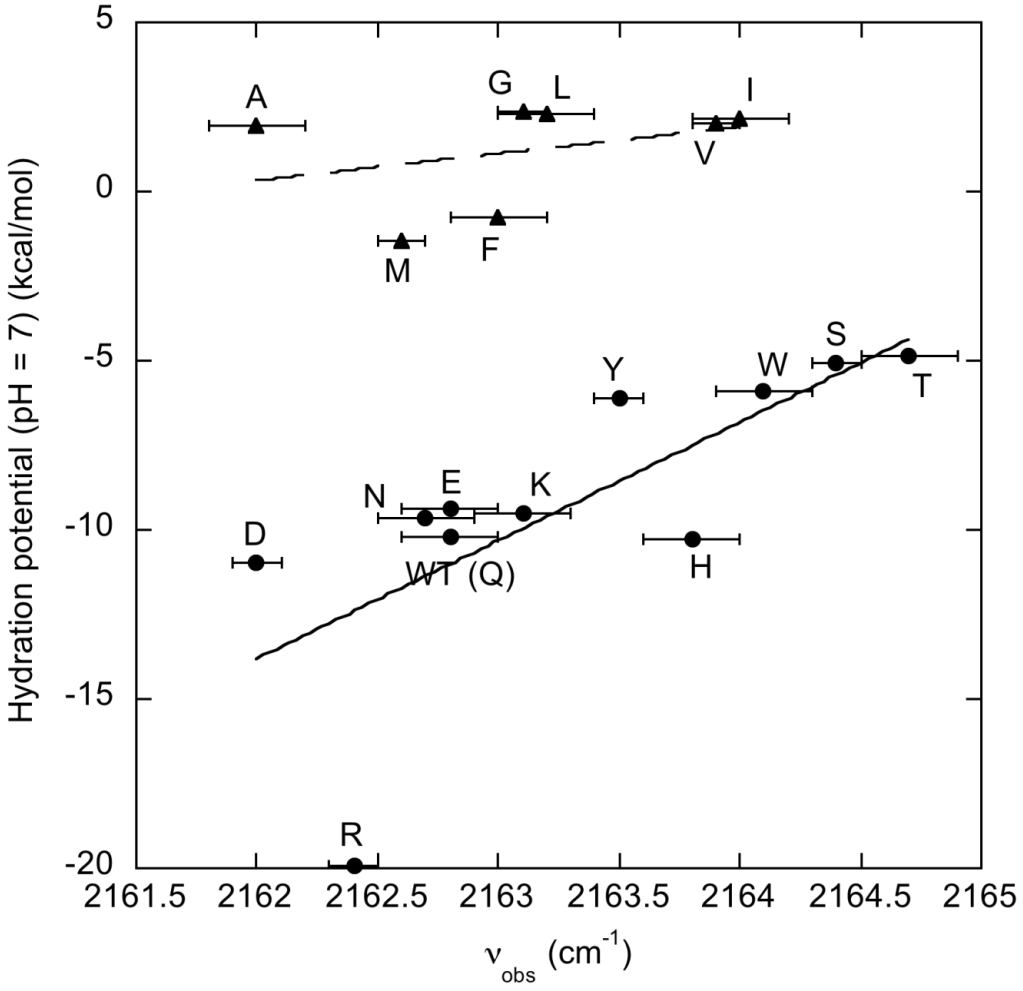

Figure 5-3 Comparison of side chain hydration potential with absorption energies

Hydration potential for amino acid side chains compiled from Ref. 68 versus measured ν_{obs} of Ralβ I18C$_{SCN}$ docked with Ras Q61X mutants. Circles: hydrophilic residues, r = 0.72 (solid line); triangles: hydrophobic residues, r = 0.34 (dashed line). Error bars on ν_{obs} represent one standard deviation from multiple measurements.

References

(1) Gottfried, D. S.; Steffen, M. A.; Boxer, S. G. *Biochim Biophys Acta* **1991**, *1059*, 76.
(2) Sitkoff, D.; Lockhart, D. J.; Sharp, K. A.; Honig, B. *Biophys J* **1994**, *67*, 2251.
(3) Bublitz, G. U.; Boxer, S. G. *Annu Rev Phys Chem* **1997**, *48*, 213.
(4) Andrews, S. S.; Boxer, S. G. *J Phys Chem A* **2000**, *104*, 11853.
(5) Fafarman, A. T.; Webb, L. J.; Chuang, J. I.; Boxer, S. G. *J Am Chem Soc* **2006**, *128*, 13356.
(6) Gallicchio, E.; Andrec, M.; Felts, A. K.; Levy, R. M. *J. Phys. Chem. B* **2005**, *109*, 6722.
(7) Chang, E. H.; Gonda, M. A.; Ellis, R. W.; Scolnick, E. M.; Lowy, D. R. *P Natl Acad Sci-Biol* **1982**, *79*, 4848.
(8) Malumbres, M.; Barbacid, M. *Nat Rev Cancer* **2003**, *3*, 459.
(9) Bos, J. L. *Cancer Research* **1989**, *49*, 4682.
(10) Berndt, N.; Hamilton, A. D.; Sebti, S. M. *Nat Rev Cancer* **2011**, *11*, 775.
(11) Downward, J. *Nat Med* **2008**, *14*, 1315.
(12) Krauss, G. *Biochemistry of signal transduction and regulation*; 3rd ed.; Wiley-VCH: Weinheim Great Britain, 2003.
(13) Wittinghofer, A.; Nassar, N. *Trends Biochem Sci* **1996**, *21*, 488.
(14) Campbell, S. L.; Khosravi-Far, R.; Rossman, K. L.; Clark, G. J.; Der, C. J. *Oncogene* **1998**, *17*, 1395.
(15) Block, C.; Janknecht, R.; Herrmann, C.; Nassar, N.; Wittinghofer, A. *Nat. Struct. Biol.* **1996**, *3*, 244.
(16) Vetter, I. R.; Linnemann, T.; Wohlgemuth, S.; Geyer, M.; Kalbitzer, H. R.; Herrmann, C.; Wittinghofer, A. *Febs Lett* **1999**, *451*, 175.
(17) Wang, J.; Yuan, Y. Z.; Zhou, Y.; Guo, L. H.; Zhang, L. Q.; Kuai, X. Z.; Deng, B. W.; Pan, Z.; Li, D.; He, F. C. *J Proteome Res* **2008**, *7*, 3879.
(18) Mor, A.; Philips, M. R. *Annu Rev Immunol* **2006**, *24*, 771.
(19) Ayllon, V.; Rebollo, A. *Mol Membr Biol* **2000**, *17*, 65.
(20) Herrmann, C.; Horn, G.; Spaargaren, M.; Wittinghofer, A. *J Biol Chem* **1996**, *271*, 6794.
(21) Herrmann, C.; Nassar, N. *Prog Biophys Mol Bio* **1996**, *66*, 1.
(22) Stafford, A. J.; Ensign, D. L.; Webb, L. J. *J. Phys. Chem. B* **2010**, *114*, 15331.
(23) Kaur, H.; Park, C. S.; Lewis, J. M.; Haugh, J. M. *Biochem J* **2006**, *393*, 235.
(24) Pacold, M. E.; Suire, S.; Perisic, O.; Lara-Gonzalez, S.; Davis, C. T.; Walker, E. H.; Hawkins, P. T.; Stephens, L.; Eccleston, J. F.; Williams, R. L. *Cell* **2000**, *103*, 931.
(25) Altschul, S. F.; Madden, T. L.; Schaffer, A. A.; Zhang, J.; Zhang, Z.; Miller, W.; Lipman, D. J. *Nucleic Acids Res* **1997**, *25*, 3389.

(26) Nassar, N.; Horn, G.; Herrmann, C.; Block, C.; Janknecht, R.; Wittinghofer, A. *Nat. Struct. Biol.* **1996**, *3*, 723.
(27) Huang, L.; Hofer, F.; Martin, G. S.; Kim, S. H. *Nat. Struct. Biol.* **1998**, *5*, 422.
(28) Huang, L.; Hofer, F.; Martin, G. S.; Kim, S. H. *Nat. Struct. Biol.* **1998**, *5*, 422.
(29) Ragain, C. M.; Newberry, R. W.; Webb, L. J. *Abstr Pap Am Chem S* **2011**, *241*.
(30) Walker, D. M.; Hayes, E. C.; Webb, L. J. *Phys Chem Chem Phys* **2013**, *15*, 12241.
(31) Ensign, D. L.; Webb, L. J. *Proteins* **2011**, *79*, 3511.
(32) D.A. Case, T. A. D., T.E. Cheatham, III, C.L. Simmerling, J. Wang, R.E. Duke, R. Luo, R.C. Walker, W. Zhang, K.M. Merz, B.P. Roberts, B. Wang, S. Hayik, A. Roitberg, G. Seabra, I. Kolossváry, K.F. Wong, F. Paesani, J. Vanicek, J. Liu, X. Wu, S.R. Brozell, T. Steinbrecher, H. Gohlke, Q. Cai, X. Ye, J. Wang, M.-J. Hsieh, G. Cui, D.R. Roe, D.H. Mathews, M.G. Seetin, C. Sagui, V. Babin, T. Luchko, S. Gusarov, A. Kovalenko, and P.A. Kollman University of California, San Francisco, 2010.
(33) Van der Spoel, D.; Lindahl, E.; Hess, B.; Groenhof, G.; Mark, A. E.; Berendsen, H. J. C. *J Comput Chem* **2005**, *26*, 1701.
(34) Mahoney, M. W.; Jorgensen, W. L. *J Chem Phys* **2000**, *112*, 8910.
(35) Mancias, J. D.; Goldberg, J. *Embo J* **2008**, *27*, 2918.
(36) Schrodinger, LLC 2010.
(37) Horton, J. R.; Sawada, K.; Nishibori, M.; Cheng, X. *J Mol Biol* **2005**, *353*, 334.
(38) Gohlke, H.; Kiel, C.; Case, D. A. *J Mol Biol* **2003**, *330*, 891.
(39) Ensign, D. L.; Webb, L. J. *Proteins* **2011**, DOI 10.1002/prot.23095 (published online 13 July 2011).
(40) Duan, Y.; Wu, C.; Chowdhury, S.; Lee, M. C.; Xiong, G.; Zhang, W.; Yang, R.; Cieplak, P.; Luo, R.; Lee, T.; Caldwell, J. W.; Wang, J.; Kollman, P. A. *J. Comput. Chem.* **2003**, *24*, 1999.
(41) Stafford, A. J.; Ensign, D. L.; Webb, L. J. *J. Phys. Chem. B* **2010**, *114*, 15331.
(42) van der Spoel, D.; Lindahl, E.; Hess, B.; Groenhof, G.; Mark, A. E.; Berendsen, H. J. C. *J. Comput. Chem.* **2005**, *26*, 1701.
(43) Jorgensen, W. L.; Chandrasekhar, J.; Madura, J. D.; Impey, R. W.; Klein, M. L. *J. Chem. Phys.* **1983**, *79*, 926.
(44) Gallicchio, E.; Andrec, M.; Felts, A. K.; Levy, R. M. *J. Phys. Chem. B* **2005**, *109*, 6722.
(45) Roux, B. *Comp. Phys. Commun.* **1995**, *91*, 275.
(46) Ragain, C. M.; Newberry, R. W.; Ritchie, A. W.; Webb, L. J. *J. Phys. Chem. B* **2012**, *116*, 9326.

(47) Chung, J. K.; Thielges, M. C.; Lynch, S. R.; Fayer, M. D. *J. Phys. Chem. B* **2012**, *116*, 11024.
(48) Stafford, A. J.; Walker, D. M.; Webb, L. J. *Biochemistry* **2012**, *51*, 2757.
(49) Choi, J. H.; Cho, M. *J Chem Phys* **2011**, *134*.
(50) Reimers, J. R.; Hall, L. E. *J Am Chem Soc* **1999**, *121*, 3730.
(51) Oh, K. I.; Choi, J. H.; Lee, J. H.; Han, J. B.; Lee, H.; Cho, M. *J Chem Phys* **2008**, *128*.
(52) Dell'Orco, D. *Mol Biosyst* **2009**, *5*, 323.
(53) Cox, A. D.; Der, C. J. *Oncogene* **2003**, *22*, 8999.
(54) Fafarman, A. T.; Sigala, P. A.; Herschlag, D.; Boxer, S. G. *J Am Chem Soc* **2010**, *132*, 12811.
(55) Silverman, L. N.; Pitzer, M. E.; Ankomah, P. O.; Boxer, S. G.; Fenlon, E. E. *J. Phys. Chem. B* **2007**, *111*, 11611.
(56) Krauss, G. *Biochemistry of Signal Transduction and Regulation*; 3 ed.; WILEY-VCH Verlag: Weinheim, Germany, 2003.
(57) Downward, J. *Nature Canc. Rev.* **2002**, *3*, 11.
(58) Eisenberg, S.; Henis, Y. I. *Cell. Sig.* **2008**, *20*, 31.
(59) Pacold, M. E.; Suire, S.; Perisic, O.; Lara-Gonzalez, S.; Davis, C. T.; Walker, E. H.; Hawkins, P. T.; Stephens, L.; Eccleston, J. F.; Williams, R. L. *Cell* **2000**, *103*, 931.
(60) Scheffzek, K.; Ahmadian, M. R.; Kabsch, W.; Wiesmuller, L.; Lautwein, A.; Schmitz, F.; Wittinghofer, A. *Science* **1997**, *277*, 333.
(61) Eccleston, J. F.; Moore, K. J. M.; Morgan, L.; Skinner, R. H.; Lowe, P. N. *J Biol Chem* **1993**, *268*, 27012.
(62) Schweins, T.; Geyer, M.; Scheffzek, K.; Warshel, A.; Kalbitzer, H. R.; Wittinghofer, A. *Nat. Struct. Biol.* **1995**, *2*, 36.
(63) Ford, B.; Hornak, V.; Kleinman, H.; Nassar, N. *Structure* **2006**, *14*, 427.
(64) Buhrman, G.; Holzapfel, G.; Fetics, S.; Mattos, C. *Proc. Natl. Acad. Sci.* **2010**, *107*, 4931.
(65) Frech, M.; Darden, T. A.; Pedersen, L. G.; Foley, C. K.; Charifson, P. S.; Anderson, M. W.; Wittinghofer, A. *Biochemistry* **1994**, *33*, 3237.
(66) Shurki, A.; Warshel, A. *Proteins* **2004**, *55*, 1.
(67) Wimley, W. C.; Creamer, T. P.; White, S. H. *Biochemistry* **1996**, *35*, 5109.
(68) Wolfenden, R.; Andersson, L.; Cullis, P. M.; Southgate, C. C. B. *Biochemistry* 1981, 20, 849.